
Analytical and numerical investigation of non-uniform straining and subgrain initiation in bicrystals in channel die compression

S.-C. Wu and K. S. Havner

Phil. Trans. R. Soc. Lond. A 1997 **355**, 1905-1943

doi: 10.1098/rsta.1997.0095

Email alerting service

Receive free email alerts when new articles cite this article - sign up in the box at the top right-hand corner of the article or click [here](#)

To subscribe to *Phil. Trans. R. Soc. Lond. A* go to: <http://rsta.royalsocietypublishing.org/subscriptions>

Analytical and numerical investigation of non-uniform straining and subgrain initiation in bicrystals in channel die compression

BY S.-C. WU[†] AND K. S. HAVNER

*Department of Civil Engineering, North Carolina State University,
Raleigh, NC 27695, USA*

Contents

	PAGE
1. Introduction	1906
2. General equations and rigid–plastic model	1907
(a) Yield locus in lattice stress space	1909
(b) Kinematics of the rigid–plastic crystal	1911
(c) Normality constraints	1911
3. Exact stress states and velocity fields	1912
(a) Determination of stress states	1912
(b) Determination of velocity fields	1915
(c) Analysis of range III ($1 > b > 0$)	1920
(d) Crystals separating from channel walls ($54.74^\circ < \phi < 72.07^\circ$)	1922
(e) Tangential velocity discontinuities	1925
(f) Initiation of subgrains: the basic solution	1926
4. Comparison with elastoplastic finite element solutions	1930
(a) Finite element model	1930
(b) Comparisons of analytical and numerical results	1931
5. Summary and discussion	1939
References	1942

Effects of the grain boundary (i.e. interface plane) on deformation and stress state in symmetric face-centred-cubic bicrystals are investigated. The full range of lattice constraint directions for crystals compressed in a (110) direction within a rigid channel die is considered. The spatial non-uniformity is only two dimensional and in the plane transverse to the loading direction. Principal analytical results are that subgrains begin to form within each crystal and tangential velocity discontinuities extend from interface edges in characteristic directions which depend on crystal orientation. Numerical (finite element) results for several orientations at the end of the elastoplastic transition from purely elastic to fully plastic (multiple-slip) response are compared with the analytical rigid–plastic solutions. Both analytical and numerical results predict subranges of lattice orientations in which there is separation of crystal and channel wall.

[†] Present address: Tamarack Technologies Inc., Mechanical Department, Science-Based Industrial Park, Hsin-Chu, Taiwan.

1. Introduction

From detailed analyses by Bay *et al.* (1989), Hughes & Nix (1989) and Bay *et al.* (1992) of many transmission electron microscope (TEM) micrographs, among other experimental studies, it is evident that the process of plastic deformation in cell-forming polycrystalline metals (which include pure aluminium and nickel and nickel-cobalt alloys) is characterized by the following microstructural evolution.

- (i) Individual grains subdivide into differently oriented crystal volumes called ‘cell blocks’, essentially parallelepipeds in shape, ‘which deform by fewer slip systems than specified by the Taylor criterion for strain accommodation’ (Bay *et al.* 1991, p.207).
- (ii) Cell blocks are separated by dense dislocation walls and microbands, across which the combination and number of active slip systems changes; the cell blocks in turn are subdivided into ordinary dislocation cells of only slight misorientation. (See the ‘Overview’ article by Bay *et al.* (1992) for descriptions and schematic representations of these microstructural features, as well as for numerous TEM micrographs.)
- (iii) Both cell blocks and ordinary cells decrease in size with increasing strain (that is, subdivision continues to occur).

Hughes (1993) has shown that there is an analogous microstructural evolution during the plastic deformation of a non-cell forming aluminium–magnesium alloy (specifically, Al+5.5 at % Mg). Single-walled boundaries, some of which develop into double-walled microbands, separate differently oriented domains of Taylor lattices (composed of approximately uniform arrays of parallel dislocations of alternating sign). Misorientations across domain boundaries may be as great as 15° at large strains and ‘Each misoriented region...slips with a different selection of slip systems than its neighbor’ (Hughes 1993, p. 1428). Hughes calls both the dense dislocation walls/microbands in cell-forming metals and the domain boundaries in non-cell forming metals ‘geometrically necessary boundaries’, which develop as a consequence of strain accommodation. A notable difference between these cases, however, is that, in the latter, the domain boundaries (including microbands) form essentially parallel to $\{111\}$ planes whereas, in cell-forming metals, the dense dislocation walls and microbands are not correlated with crystallographic slip planes.

A general analysis of all of these phenomena from a continuum crystallographic slip perspective (that is, using crystal mechanics) is not achievable. (Obviously, an understanding of dislocation generation or annihilation, in Taylor lattices, dense dislocation walls, or otherwise, is not accessible via crystal mechanics alone.) Nonetheless, in Wu & Havner (1995), we found that by analysing one of the most basic experimental configurations in which the above phenomena may be expected to occur (bicrystals in channel die compression), two apparent microstructural features—the delineation of (geometrically) necessary interior boundaries and the initiation of subgrains—can be rigorously predicted mathematically.

In both Wu & Havner (1995) and the present work, subgrain initiation is defined as the subdivision of crystals into regions of finitely differing lattice-rotation rates (with the onset of fully plastic response). This subdivision takes place in a rigid–plastic crystal model at the yield point and is a consequence of the mathematical analysis of slip-system kinematics, crystal yield locus and stress and geometric boundary conditions.

The configuration investigated here and in our previous work, first advocated in Havner *et al.* (1994) as a non-uniform deformation problem particularly worthy of study, is a symmetric face-centred-cubic (FCC) bicrystal having (110) lattice planes

normal to the compressive loading direction and an interface plane of mirror symmetry transverse to the channel axis. We review the theoretical and experimental basis for treating this problem as one of only two-dimensional spatial non-uniformity in §2 and give the requisite general equations for analysis.

In Wu & Havner (1995), the governing pairs of hyperbolic partial differential equations for stress and velocity fields in a rigid–plastic crystal at the yield point are solved analytically for all lateral constraint directions between lattice directions $[00\bar{1}]$ and $[\bar{1}\bar{1}\bar{2}]$, a range of 35.26° . It is established that both tangential velocity discontinuities and the initiation of subgrains in the bicrystal model are consequences of the boundary conditions and yield-locus normality constraints. In §3, the heart of the present work, we both encompass and substantially extend that investigation by carrying out a comprehensive analysis of the full 90° range of crystal orientations in (110) channel die compression.

During the elastoplastic transition stage between purely elastic response and the onset of finite multiple slipping (when lattice strain increments may be disregarded), the governing equations can be elliptic. Using the finite element method, in §4 we numerically investigate this stage for particular orientations and compare the final incremental response with our analytical solutions. In certain cases, the results are quite close (although the adopted finite element model does not admit tangential velocity discontinuities).

The principal analytical results, numerical comparisons and possible insights are summarized in §5, along with additional discussion. Analytically, the crystals begin to subdivide into distinct regions defined by characteristic directions, and tangential velocity discontinuities (interpreted as the initiation of shear bands) extend from the intersections of the bicrystal interface with the lateral surfaces. Both analytically and numerically, there are ranges of lattice orientations in (110) compression in which the bicrystal separates from one or both channel walls along all, or part, of its length. This prediction awaits experimental confirmation (or refutation).

2. General equations and rigid–plastic model

Consider the initial configuration of a symmetric bicrystal in (110) channel die compression, shown in plan view in figure 1, with each crystal a ‘unit cube’ to an appropriate scale. We assume the contact surfaces between bicrystal and rigid die (faces $y = 0, 1$ and $x = 0$) and between bicrystal and rigid workpiece (face $x = 1$) are smooth and well lubricated (by Teflon coating, or otherwise) and may be treated as ideally frictionless. We also assume perfect bonding between crystals at their interface ($z = 0$). Consequently, the initial stress boundary conditions for the right-hand side are:

$$\left. \begin{aligned} x = 0, 1: \quad \sigma_{xy} = \sigma_{xz} = 0, \quad \sigma_{xx} \leq 0, \\ y = 0, 1: \quad \sigma_{xy} = \sigma_{yz} = 0, \quad \sigma_{yy} \leq 0, \\ z = 0: \quad \sigma_{xz} = \sigma_{yz} = 0, \\ z = 1: \quad \sigma_{xz} = \sigma_{yz} = \sigma_{zz} = 0. \end{aligned} \right\} \quad (2.1)$$

Furthermore, X -direction displacements are zero on face $x = 0$ and uniform (prescribed) on face $x = 1$, Y -direction displacements are zero† on faces $y = 0, 1$ and Z -direction displacements are zero at the interface $z = 0$.

† We shall need to reconsider this condition for a particular range of lattice orientations in §3 c.

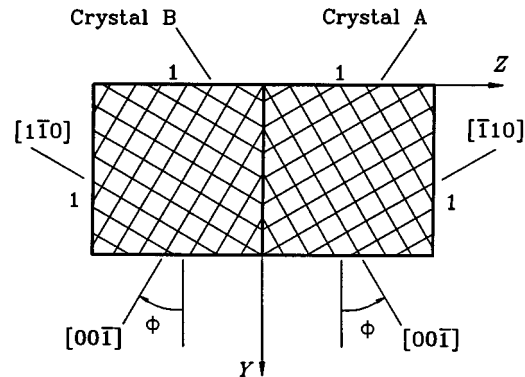


Figure 1. Initial configuration of symmetric bicrystal in (110) channel die compression as viewed from loading direction. (Rectangular grid represents underlying lattice.)

For a cubic lattice in (110) compression and the preceding boundary conditions, Fuh (1989, §4.1) found that the initial elastic problem reduces to one of generalized plane strain, because of the form taken by the elastic stiffness matrix on channel axes. Consequently, lattice strains ε_{xy} , ε_{xz} and stresses σ_{xy} , σ_{xz} are zero, ε_{xx} is uniform and there is spatial non-uniformity of the other strains only with respect to the Y and Z -directions. Moreover, Wu (1995, §5.2) has shown that the incremental elastoplastic stiffness matrix for f.c.c. crystals in this configuration has the same form as the elastic stiffness matrix during the (small strain) elastoplastic transition stage. (This is the stage from the end of purely elastic response up to the limit state, at which point the crystals can deform finitely by multiple slip and lattice straining becomes negligible (see Havner (1992, §5.4) for an analysis of single crystals at this stage.) Thus, the problem of symmetric bicrystals in (110) loading reduces to a two-dimensional one throughout the elastoplastic transition as well. This reduction also has been confirmed numerically by Wu (1995), who began with a fully three-dimensional finite element model.

In all experiments involving large strains of *single* FCC crystals in (110) channel die compression of which we are aware, the crystal finitely sheared only in the horizontal plane perpendicular to the loading direction X (with the exception of two singular orientations, in which crystals deformed rectangularly) and the lattice either rotated about that axis or was stable relative to the channel axes (Chin *et al.* 1966; Wonsiewicz & Chin 1970; Wonsiewicz *et al.* 1971; Kocks & Chandra 1982; Driver & Skalli 1982; Skalli *et al.* 1983; Skalli 1984). Moreover, the gross distortions in these experiments were highly uniform to logarithmic compressive strains of order 1, as may be seen from photographs of finitely deformed FCC crystals in Chin *et al.* (1966, figure 9) and Driver & Skalli (1982, figure 5), among others. This experimental behaviour of single crystals to large strains has been accounted for theoretically, for the full range of initial channel constraint directions relative to the lattice, both according to various hardening rules (Sue & Havner 1984; Havner & Sue 1985; Fuh & Havner 1986; Havner & Chidambarrao 1987; Chidambarrao & Havner 1988*a, b*) and by the theory of minimum plastic spin (Fuh & Havner 1989). (See Havner (1992, chapter 5) for a comprehensive review of both theory and experiment in channel die compression of single crystals.)

Because single crystals in (110) channel die compression free to shear in both vertical (XZ) and horizontal (YZ) longitudinal planes do so only in the latter plane, with accompanying lattice rotation only about the loading direction X , it follows

(as argued in Havner *et al.* (1994) and Wu & Havner (1995)) that the spatial non-uniformity of deformation of adequately lubricated bicrystals may be anticipated as being two dimensional, rather than three (at least to moderate strains). That is, geometric incompatibility between differently oriented, freely shearing individual crystals in (110) loading exists only in YZ planes, hence the non-uniform straining necessary to satisfy compatibility in bicrystals logically should take place entirely within those planes. This perspective is fully consistent with the theoretical elastic and elastoplastic transition response discussed above.

For the foregoing reasons, we consider the general problem of symmetric bicrystals in (110) channel die compression to reduce to a two-dimensional one governed by the following equilibrium and kinematic relations:

$$\sigma_{xy} = \sigma_{xz} = 0, \quad d_{xy} = d_{xz} = 0, \quad \omega_y = \omega_z = 0, \quad w_y = w_z = 0, \quad (2.2)$$

$$\sigma_{xx} \leq 0, \quad \frac{\partial \sigma_{yy}}{\partial y} + \frac{\partial \sigma_{yz}}{\partial z} = 0, \quad \frac{\partial \sigma_{yz}}{\partial y} + \frac{\partial \sigma_{zz}}{\partial z} = 0, \quad (2.3)$$

$$d_{xx} = -1, \quad d_{yy} = \frac{\partial v}{\partial y}, \quad 2d_{yz} = \frac{\partial w}{\partial y} + \frac{\partial v}{\partial z}, \quad d_{zz} = \frac{\partial w}{\partial z}, \quad 2w_x = \frac{\partial w}{\partial y} - \frac{\partial v}{\partial z}, \quad (2.4)$$

where velocities $u = -x$, $v(y, z)$ and $w(y, z)$ and lattice-rotation rate $\omega_x = \phi'(y, z)$ are defined with respect to logarithmic compressive strain e_L (the prime indicating this differentiation) rather than with respect to time. The d_{ij} are components of Eulerian strain-rate D and $\boldsymbol{\omega} = (\omega_x, \omega_y, \omega_z)^T$ and $\boldsymbol{w} = (w_x, w_y, w_z)^T$ are axial vectors of the lattice and material spin tensors $\boldsymbol{\omega}$ and \boldsymbol{W} , respectively, relative to the channel axes. ($e_L = \ln(1/\lambda)$, with λ the spacing stretch in loading direction X ; whence $\lambda_0 = 1$.) Correspondingly, the reduced boundary conditions for the right-hand crystal (figure 1) are:

$$\left. \begin{aligned} x = 0: \quad u = 0, \quad x = 1: \quad u = -1, \\ y = 0, 1: \quad \sigma_{yz} = 0, \quad v = 0, \\ z = 0: \quad \sigma_{yz} = 0, \quad w = 0; \quad z = 1: \quad \sigma_{yz} = \sigma_{zz} = 0. \end{aligned} \right\} \quad (2.5)$$

We take these equations to apply at the outset of fully plastic response (finite multiple-slipping) as well as throughout the infinitesimal strain, elastoplastic transition stage.

(a) Yield locus in lattice stress space

From $\sigma_{xy} = \sigma_{xz} = 0$ and the standard stress transformation between channel die and $[100]$, $[010]$, $[001]$ lattice axes in (110) compression, we find (Havner *et al.* 1994, equations (3.1)₁, (3.1)₃, and (5.2)₁)

$$\sigma_{11} = \sigma_{22}, \quad \sigma_{13} = -\sigma_{23}, \quad \sigma_{11} + \sigma_{12} = \sigma_{xx} \quad (2.6)$$

(with σ_{ij} , $i, j = 1, 2, 3$, the lattice components of Cauchy stress). Consequently, the resolved shear stresses on the 12 FCC slip systems of table 1 are given by

$$\tau_k = (b_3 n_3)_k (\sigma_{33} - \sigma_{11}) + (b_1 n_2 + b_2 n_1)_k \sigma_{12} + \{(b_1 - b_2)n_3 + b_3(n_1 - n_2)\} \sigma_{13}, \quad (2.7)$$

where \boldsymbol{b}_k , \boldsymbol{n}_k are unit vectors in the slip and normal directions of the k th slip system. The systems are numbered as follows:

$$\begin{aligned} a\bar{1}, b\bar{2} = 1, 2, \quad c\bar{1}, c\bar{2} = 3, 4, \quad a\bar{3}, b\bar{3} = 5, 6, \\ d\bar{1}, d\bar{2} = 7, 8, \quad a\bar{2}, b\bar{1} = 9, 10, \quad c\bar{3}, d\bar{3} = 11, 12 \end{aligned}$$

Table 1. Designation of slip systems in FCC crystals

plane	(111)			(11 $\bar{1}$)			(1 $\bar{1}\bar{1}$)			(1 $\bar{1}$ 1)		
direction	0 $\bar{1}$ 1	10 $\bar{1}$	$\bar{1}$ 10	0 $\bar{1}\bar{1}$	101	$\bar{1}$ 10	01 $\bar{1}$	101	$\bar{1}\bar{1}$ 0	011	10 $\bar{1}$	$\bar{1}\bar{1}$ 0
system	a1	a2	a3	b1	b2	b3	c1	c2	c3	d1	d2	d3

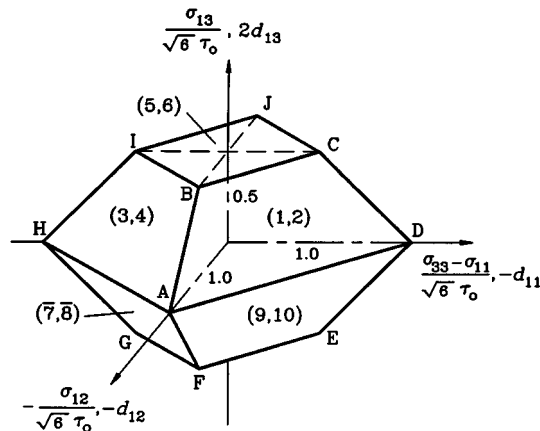


Figure 2. Initial yield locus in lattice stress space, with slip systems indicated in parentheses.

(the bar above signifying the opposite-sense system from that in the table). Thus, disregarding the very small effects of lattice straining on slip-system geometry, we have

$$\left. \begin{aligned} \tau_1 = \tau_2 = A + B + C, \quad \tau_3 = \tau_4 = -A + B + C, \\ \tau_5 = \tau_6 = 2B, \quad \tau_7 = \tau_8 = A + B - C, \\ \tau_9 = \tau_{10} = A - B + C, \quad \tau_{11} = \tau_{12} = 0, \\ A = (1/\sqrt{6})(\sigma_{33} - \sigma_{11}), \quad B = (1/\sqrt{6})\sigma_{13}, \quad C = -(1/\sqrt{6})\sigma_{12}. \end{aligned} \right\} \quad (2.8)$$

Following the arguments in Havner *et al.* (1994, p. 366), we consider the changes in critical resolved shear stresses, or ‘critical strengths’, to be small during the elasto-plastic transition stage and the effects of any anisotropy in hardening to be insignificant. Therefore, *Schmid’s law* of (uniform) critical shear stress is taken to hold in all systems, both active and latent, throughout this stage. Let τ_0 denote the critical strength at the beginning of fully plastic response. The yield locus in three-dimensional lattice stress space $\sigma_{33} - \sigma_{11}(\sqrt{6}A)$, $\sigma_{13}(\sqrt{6}B)$ and $\sigma_{12}(\sqrt{6}C)$ is then defined by the five pairs of planes:

$$\left. \begin{aligned} A + B + C = \pm\tau_0, \quad -A + B + C = \pm\tau_0, \quad 2B = \pm\tau_0, \\ A + B - C = \pm\tau_0, \quad A - B + C = \pm\tau_0. \end{aligned} \right\} \quad (2.9)$$

The corresponding decahedron, shown in figure 2, has five planes of symmetry ($A = 0$, $B = 0$, $C = 0$, $A + C = 0$ and $A - C = 0$), with slip systems activated in pairs, corresponding to the numbers on the faces.

(b) Kinematics of the rigid-plastic crystal

In fully plastic response (finite multiple-slipping), lattice strain-rates are negligible compared with plastic strain-rates and we adopt a rigid-plastic crystal model. Accordingly, the Eulerian strain-rate D and plastic spin $\Omega = W - \omega$ are given by

$$D = \text{sym} \sum (\mathbf{b} \otimes \mathbf{n})_k \gamma'_k, \quad \Omega = \text{skw} \sum (\mathbf{b} \otimes \mathbf{n})_k \gamma'_k, \quad (2.10)$$

where γ'_k is the crystallographic slip-rate (with respect to logarithmic compressive strain e_L) in the k th slip system. From $d_{xy} = d_{xz} = 0$, and the strain-rate transformation between channel and lattice axes, we necessarily have, analogous to (2.6),

$$d_{11} = d_{22}, \quad d_{13} = -d_{23}, \quad d_{11} + d_{12} = d_{xx} = -1, \quad (2.11)$$

which give three constraints on the 10 possible non-zero γ'_k from (2.10)₁. (Note that $\gamma'_{11} = \gamma'_{12} = 0$ from (2.8)₆.) In addition, from the transformation of the axial vector \mathbf{a}_Ω of plastic spin Ω , we find

$$a_1 \equiv \Omega_{32} = a_2 \equiv \Omega_{13} = (1/\sqrt{2})a_x, \quad a_3 = 0 \quad (2.12)$$

(with $a_x = w_x - \phi'$), corresponding to lattice spin only about the (110) loading direction X . Equations (2.12) give two more constraints on the slip rates from (2.10)₂. Thus, from (2.10)–(2.12), we have the five constraints (Wu & Havner 1995, equations (2.11))

$$\gamma'_1 + \gamma'_5 = \gamma'_2 + \gamma'_6, \quad \gamma'_3 = \gamma'_4, \quad \gamma'_7 = \gamma'_8, \quad \gamma'_1 + \gamma'_9 = \gamma'_2 + \gamma'_{10} = \frac{1}{2}\sqrt{6}, \quad (2.13)$$

from which the strain-rate components on lattice axes simplify to (Havner *et al.* 1994, equations (4.10))

$$\left. \begin{aligned} d_{11} = d_{22} &= -\frac{1}{2}d_{33} = -\frac{1}{2} + (1/\sqrt{6})(\gamma'_3 - \gamma'_7), \\ d_{13} = -d_{23} &= -\frac{1}{4} + (1/(2\sqrt{6}))(2\gamma'_1 + \gamma'_3 + 2\gamma'_5 + \gamma'_7), \\ d_{12} &= -\frac{1}{2} - (1/\sqrt{6})(\gamma'_3 - \gamma'_7), \end{aligned} \right\} \quad (2.14)$$

with all non-zero γ'_k dependent upon y and z .

(c) Normality constraints

We now connect the pure multiple-slip kinematics of the preceding section (§2b) with the yield locus of §2a and give the normality constraints on strain-rates for the rigid-plastic crystal.

From the fourth and fifth equations of (2.13), it is evident that at least one of systems 1 (a1) and 9 (a $\bar{2}$), and one of their yield-locus pairs 2 (b $\bar{2}$) and 10 (b1), must be active in the positive sense. Thus, all stress states in the crystal must lie on face ABCD (systems 1, 2) or face ADEF (systems 9, 10) of the yield locus, including edges and vertices, no matter what the initial lattice orientation ϕ_0 (Havner *et al.* 1994, p. 368). It follows that no one of these four systems can be active in the negative sense. Furthermore, from the lower bound analysis of the yield point load in Havner *et al.* (1994, §5), we conclude (following Wu & Havner (1995, §3)) that σ_{13} is non-negative for all ϕ_0 . Thus, all stress states will lie on face ABCD. Wu (1995) found this to be the case for every crystal point, throughout the elastoplastic transition, from finite element calculations of five different bicrystal orientations spanning the range 0 to 90°. Consequently, consideration of the yield locus (figure 2) may be reduced to the single face ABCD and its edges and vertices.

The generalized normality constraints on Eulerian strain rates correspond to

$$\tau_k \gamma'_k \geq 0 \quad (\text{no sum}), \quad |\tau_k| = \tau_0, \quad (2.15)$$

in every critical slip system, and can be worked-out from (2.8) and (2.14) or directly from the geometry of face ABCD and adjacent faces of the yield locus. They are (Havner *et al.* 1994, equations (7.9); Wu & Havner 1995 equations (2.8))

$$\left. \begin{array}{l} \text{vertex A: } -2d_{12} \geq 1, \quad -d_{12} \geq 2d_{13} \geq d_{12}, \\ \text{vertex B: } -2d_{12} \geq 1, \quad -d_{12} \leq 2d_{13}, \\ \text{vertex C: } -2d_{12} \geq 1, \quad -d_{11} \leq 2d_{13}, \\ \text{vertex D: } -2d_{11} \geq 1, \quad -d_{11} \geq 2d_{13} \geq d_{11}, \\ \text{vertex AB: } -2d_{12} \geq 1, \quad -d_{12} = 2d_{13}, \\ \text{vertex BC: } d_{11} = d_{12} = -\frac{1}{2}, \quad -d_{12} \leq 2d_{13}, \\ \text{vertex CD: } -2d_{11} \geq 1, \quad -d_{11} = 2d_{13}, \\ \text{edge AD: } d_{11} = d_{12} = -\frac{1}{2}, \quad -d_{12} \geq 2d_{13} \geq d_{12}, \\ \text{face ABCD: } d_{11} = d_{12} = -2d_{13}. \end{array} \right\} \quad (2.16)$$

(The face excludes vertices and edges, and the edges exclude vertices.)

3. Exact stress states and velocity fields

In this section, we present a comprehensive, analytical investigation of the yield point state for symmetric bicrystals in (110) loading that encompasses the following three ranges of channel constraint direction Y (figure 1):

$$\begin{array}{ll} \text{range I:} & \text{between } [00\bar{1}] \text{ and } [1\bar{1}\bar{2}], \quad 0 < \phi_0 < 35.26^\circ, \\ \text{range II:} & \text{between } [1\bar{1}\bar{2}] \text{ and } [1\bar{1}\bar{1}], \quad 35.26^\circ < \phi_0 < 54.74^\circ, \\ \text{range III:} & \text{between } [1\bar{1}\bar{1}] \text{ and } [1\bar{1}0], \quad 54.74^\circ < \phi_0 < 90^\circ. \end{array}$$

(We exclude consideration of the four limit orientations $Y = [00\bar{1}]$, $[1\bar{1}\bar{2}]$, $[1\bar{1}\bar{1}]$ and $[1\bar{1}0]$, the first three of which are singular and correspond to vertices of the yield locus, figure 2.) Exact solutions for range I are developed in Wu & Havner (1995) and we follow that approach for all three ranges here. (Also, a range II solution is presented, in brief, in Havner & Wu (1995).)

(a) Determination of stress states

From the geometry of the yield locus, the equations of face ABCD and its edges are:

$$\left. \begin{array}{l} \text{AB: } \sigma_{33} = \sigma_{11}, \quad 0 \leq \sigma_{13} = \sigma_{12} + \sqrt{6}\tau_0 \leq (\sqrt{6}/2)\tau_0, \\ \text{BC: } \sigma_{13} = (\sqrt{6}/2)\tau_0, \quad 0 \leq \sigma_{33} - \sigma_{11} = \sigma_{12} + (\sqrt{6}/2)\tau_0 \leq (\sqrt{6}/2)\tau_0, \\ \text{CD: } \sigma_{12} = 0, \quad (\sqrt{6}/2)\tau_0 \leq \sigma_{33} - \sigma_{11} = \sqrt{6}\tau_0 - \sigma_{13} \leq \sqrt{6}\tau_0, \\ \text{AD: } \sigma_{13} = 0, \quad 0 \leq \sigma_{33} - \sigma_{11} = \sigma_{12} + \sqrt{6}\tau_0 \leq \sqrt{6}\tau_0, \\ \text{ABCD: } \sigma_{33} - \sigma_{11} - \sigma_{12} + \sigma_{13} = \sqrt{6}\tau_0. \end{array} \right\} \quad (3.1)$$

Motivated by the lower-bound analysis in Havner *et al.* (1994), we consider only stress states that lie along AB, BC and AD. Upon substituting the respective equations for

σ_{13} and σ_{33} from (3.1) into the stress transformation equations, and the results of that into the equilibrium equations (2.3), we obtain the following pair of hyperbolic partial differential equations governing the remaining unknown stresses σ_{11} and σ_{12} :

$$A \frac{\partial \sigma}{\partial y} + B \frac{\partial \sigma}{\partial z} = \mathbf{0}, \quad (3.2)$$

with $\sigma = (\sigma_{11}, \sigma_{12})^T$ and

$$A = \begin{bmatrix} 1 & -\frac{2(2b+1)}{b^2+2} \\ 0 & \frac{\sqrt{2}(b+2)(b-1)}{b^2+2} \end{bmatrix}, \quad B = \begin{bmatrix} 0 & \frac{\sqrt{2}(b+2)(b-1)}{b^2+2} \\ 1 & -\frac{b(b-4)}{b^2+2} \end{bmatrix} \quad \text{for edge AB,} \quad (3.3)$$

$$A = \begin{bmatrix} 1 & \frac{b^2-2}{b^2+2} \\ 0 & \frac{2\sqrt{2}b}{b^2+2} \end{bmatrix}, \quad B = \begin{bmatrix} 0 & \frac{2\sqrt{2}b}{b^2+2} \\ 1 & -\frac{b^2-2}{b^2+2} \end{bmatrix} \quad \text{for edges BC and AD,} \quad (3.4)$$

where we have used

$$b = \sqrt{2} \cot \phi. \quad (3.5)$$

Thus, the channel constraint direction may be expressed $Y = [1\bar{1}\bar{b}]$; and $0 < \phi < 90^\circ$ is equivalent to $\infty > b > 0$.

Following a standard procedure for solving first-order systems (see Chester (1971, chapter 12), for example), we determine the characteristic directions $\mu = dy/dz$ as the roots of the equation $\det(A - \mu B) = 0$ and find (from (3.3)–(3.4))

$$\mu_1 = \frac{\sqrt{2}(b-1)}{b+2}, \quad \mu_2 = -\frac{b+2}{\sqrt{2}(b-1)} \quad \text{for edge AB,} \quad (3.6)$$

$$\mu_1 = \frac{b}{\sqrt{2}}, \quad \mu_2 = -\frac{\sqrt{2}}{b} \quad \text{for edges BC and AD.} \quad (3.7)$$

Because $\mu_1\mu_2 = -1$, the corresponding directions α, β are orthogonal. Thus, we need define only the single angle θ counterclockwise from Y for the α -direction (figure 3), given by (from (3.5) and the first equations of (3.6) and (3.7))

$$\text{edge AB: } \tan \theta = \frac{b+2}{\sqrt{2}(b-1)}, \quad \theta = \phi + \tan^{-1}(1/\sqrt{2}); \quad (3.8)$$

$$\text{edges BC and AD: } \tan \theta = \sqrt{2}/b, \quad \theta = \phi. \quad (3.9)$$

Thus, for edge AB, the first characteristic direction is rotated 35.26° counterclockwise from $[00\bar{1}]$, while for the other two edges it coincides with $[00\bar{1}]$.

From the coordinate transformation between y, z and α, β (or by forming the inner product of (3.2) with the eigenvectors of μ_1 and μ_2 in turn), the governing hyperbolic equations can be expressed in the following simple canonical forms:

$$\text{edge AB: } \left\{ \begin{array}{l} d(\sigma_{11} + \sigma_{12}) = 0 \quad \text{along } \alpha\text{-lines } \frac{dy}{dz} = \cot \theta, \\ d(\sigma_{11} - 2\sigma_{12}) = 0 \quad \text{along } \beta\text{-lines } \frac{dy}{dz} = -\tan \theta, \end{array} \right\} \quad (3.10)$$

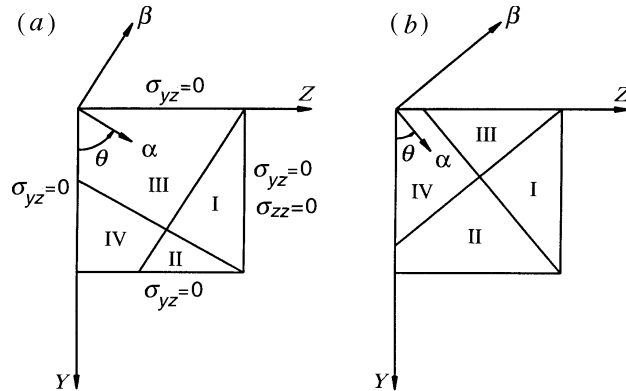


Figure 3. Stress boundary conditions in symmetric bicrystals and grain subdivision into four regions for stress analysis. (a) $90^\circ > \theta \geq 45^\circ$, (b) $45^\circ \geq \theta > 35.26^\circ$.

$$\text{edges BC and AD: } \left\{ \begin{array}{l} d(\sigma_{11} + \sigma_{12}) = 0 \quad \text{along } \alpha\text{-lines } \frac{dy}{dz} = \cot \theta, \\ d(\sigma_{11} - \sigma_{12}) = 0 \quad \text{along } \beta\text{-lines } \frac{dy}{dz} = -\tan \theta \end{array} \right\} \quad (3.11)$$

(with θ in (3.10)–(3.11) determined, respectively, by (3.8)–(3.9)). Equations (3.10) for edge AB of the yield locus first were derived in Wu & Havner (1995, equations (3.10) and (3.11)) appears in an equivalent canonical form (in terms of σ_{yy} , σ_{zz} and ϕ) in Havner & Wu (1995, equations (12)), for edge BC only.

To solve these equations we, of course, make use of the stress boundary conditions. From (3.1), (3.5) and the stress transformation equations, we have all around the vertical boundary (from $\sigma_{yz} = 0$ there)

$$\left. \begin{array}{l} \text{edge AB: } \sigma_{12} = -\sqrt{6}\tau_0 \frac{b^2 - 2}{(b+2)(b-1)}, \\ \text{edge BC: } \sigma_{12} = -\sqrt{6}\tau_0 \frac{(b+2)(b-1)}{4b}, \\ \text{edge AD: } \sigma_{12} = -(\sqrt{6}/2)\tau_0 \end{array} \right\} \quad (3.12)$$

and, on $z = 1$ (from $\sigma_{zz} = 0$ on the free face),

$$\left. \begin{array}{l} \text{edge AB: } \sigma_{11} = -\sqrt{6}\tau_0 \frac{b^2}{(b+2)(b-1)}, \\ \text{edge BC: } \sigma_{11} = -\sqrt{6}\tau_0 \frac{b^2 + b + 2}{4b}, \\ \text{edge AD: } \sigma_{11} = -(\sqrt{6}/2)\tau_0. \end{array} \right\} \quad (3.13)$$

Consider stress states lying on edge BC of the yield locus. From the second equations of (3.12) and (3.13) at $z = 1$, and (3.11) along α and β -lines, σ_{11} and σ_{12} are uniform throughout region I of figure 3. Moreover, because:

- (i) $\sigma_{11} + \sigma_{12}$ is uniform throughout regions I and III of the figure (from (3.11)₁);
- (ii) $\sigma_{11} - \sigma_{12}$ is uniform throughout regions I and II (from (3.11)₂); and
- (iii) σ_{12} is given by (3.12)₂ on the boundary,

it follows that σ_{11} and σ_{12} are those same uniform values in regions II and III. Then, following α -lines from II and β -lines from III into region IV of figure 3, one sees

that σ_{11} , σ_{12} are uniform and given by the second equations of (3.13) and (3.12) throughout the crystal, with $\sigma_{yz} = \sigma_{zz} = 0$ everywhere.

By similar arguments, one may readily establish the uniformity and biaxiality of stress states in the crystal lying on each of edges AB (Wu & Havner 1995) and AD of the yield locus. Thus, from (3.1), (3.12), (3.13), and the stress transformation equations, the yield-point load (unit area) $f_0 = -\sigma_{xx}$ and lateral constraint stress $g_0 = -\sigma_{yy}$ acting on each of the crystals are

$$\text{edge AB: } f_0 = 2\sqrt{6}\tau_0 \frac{b+1}{b+2}, \quad g_0 = \sqrt{6}\tau_0 \frac{b^2+2}{(b+2)(b-1)}, \quad (3.14)$$

$$\text{edge BC: } f_0 = \sqrt{6}\tau_0 \frac{b+1}{2}, \quad g_0 = \sqrt{6}\tau_0 \frac{b^2+2}{2b}, \quad (3.15)$$

$$\text{edge AD: } f_0 = \sqrt{\tau_0}, \quad g_0 = 0. \quad (3.16)$$

Obviously, all stress states on edge AD are at a single point (the midpoint of the line) independent of lattice orientation.

The ranges of orientations to which these solutions apply are readily determined from (3.12) and the bounds on σ_{12} in (3.1). We find

$$\begin{aligned} \text{edge AB: } & \infty \geq b \geq 2, \quad 0 \leq \phi_0 \leq 35.26^\circ, \\ \text{edge BC: } & 2 \geq b \geq 1, \quad 35.26^\circ \leq \phi_0 \leq 54.74^\circ, \\ \text{edge AD: } & 1 \geq b \geq 0, \quad 54.74^\circ \leq \phi_0 \leq 90^\circ. \end{aligned}$$

Thus, edges AB, BC and AD of the yield locus (excluding corners) respectively correspond to ranges I, II and III defined at the beginning of §3. The yield-point loads f_0 for these ranges are identical to the greatest lower bounds in Havner *et al.* (1994) obtained by simply assuming a uniform biaxial stress state.

(b) Determination of velocity fields

The normality constraints along the edges of the yield locus associated with each range of parameter b are (from (2.16))

$$\left. \begin{aligned} b > 2 \text{ (edge AB): } & -d_{12} = 2d_{13}, \quad -2d_{12} \geq 1, \\ 2 > b > 1 \text{ (edge BC): } & d_{11} = d_{12} = -\frac{1}{2}, \quad -d_{12} \leq 2d_{13}, \\ 1 > b > 0 \text{ (edge AD): } & d_{11} = d_{12} = -\frac{1}{2}, \quad -d_{12} \geq 2d_{13} \geq d_{12}. \end{aligned} \right\} \quad (3.17)$$

(Note that, for each range, these kinematic constraints permit stress states that lie on face ABCD, figure 2, away from the respective edge as well as on that edge. This will become significant later in selecting analytical solutions and comparing them with finite element results.) Upon substituting the strain-rate transformation equations (with $d_{xx} = -1$) into the equalities in (3.17), using (3.5) and the condition of isochoric flow,

$$d_{yy} + d_{zz} = 1, \quad (3.18)$$

we obtain

$$\begin{aligned} b > 2: & \quad (b^2 - 8b - 2)d_{yy} + 2\sqrt{2}(b^2 + b - 2)d_{yz} = 2(b - 1)^2, \\ 2 > b > 1 \text{ and } 1 > b > 0: & \quad (b^2 - 2)d_{yy} + 2\sqrt{2}bd_{yz} = b^2. \end{aligned} \quad (3.19)$$

Thus, from the basic kinematic relations (2.4) and (3.18)–(3.19), the velocity field $\mathbf{u} = (v, w)^T$ in the YZ plane is governed by the following pair of first-order hyperbolic

equations:

$$A_1 \frac{\partial \mathbf{u}}{\partial y} + \frac{\partial \mathbf{u}}{\partial z} = \mathbf{c}, \quad (3.20)$$

$$A_1 = \begin{bmatrix} \frac{b^2 - 8b - 2}{\sqrt{2}(b+2)(b-1)} & 1 \\ 1 & 0 \end{bmatrix}, \quad \mathbf{c} = \begin{bmatrix} \frac{\sqrt{2}(b-1)}{b+2} \\ 1 \end{bmatrix}, \quad \text{for } b > 2; \quad (3.21)$$

$$A_1 = \begin{bmatrix} \frac{b^2 - 2}{\sqrt{2}b} & 1 \\ 1 & 0 \end{bmatrix}, \quad \mathbf{c} = \begin{bmatrix} \frac{b}{\sqrt{2}} \\ 1 \end{bmatrix}, \quad \text{for } 2 > b > 1 \text{ and } 1 > b > 0. \quad (3.22)$$

It is readily found that the characteristic directions $\mu = dy/dz$ determined from $\det(A_1 - \mu I)$ are identical with those for stress, given by (3.6)–(3.7). Therefore, equations of the velocity field have the same orthogonal α , β -directions as the equilibrium equations.

Following the same procedure as before, we obtain canonical forms of (3.20) as

$$b > 2: \quad \left\{ \begin{array}{l} d \left\{ v + \frac{b+2}{\sqrt{2}(b-1)} w \right\} = \sqrt{\frac{3}{2}} \frac{\sqrt{b^2+2}}{b-1} d\alpha, \text{ along } \alpha\text{-lines } \frac{dy}{dz} = \cot \theta, \\ d \left\{ v - \frac{\sqrt{2}(b-1)}{b+2} w \right\} = 0, \text{ along } \beta\text{-lines } \frac{dy}{dz} = -\tan \theta, \end{array} \right\} \quad (3.23)$$

$2 > b > 1$ and $1 > b > 0$:

$$\left\{ \begin{array}{l} d \left\{ v + \frac{\sqrt{2}}{b} w \right\} = \frac{\sqrt{b^2+2}}{b} d\alpha, \text{ along } \alpha\text{-lines } \frac{dy}{dz} = \cot \theta, \\ d \left\{ v - \frac{b}{\sqrt{2}} w \right\} = 0, \text{ along } \beta\text{-lines } \frac{dy}{dz} = -\tan \theta, \end{array} \right\} \quad (3.24)$$

with θ again given by (3.8) for $b > 2$ (edge AB) and (3.9) for $2 > b > 1$ and $1 > b > 0$ (edges BC and AD). However, as first shown for $b > 2$ in Wu & Havner (1995), much simpler equations are achievable by choosing as dependent variables the velocity components in the α and β -directions, which we denote u_α , u_β . These equations are, for all orientation ranges in (110) channel die compression, the simple and rather elegant relations

$$du_\alpha = d\alpha \quad \text{along } \alpha\text{-lines } \frac{dy}{dz} = \cot \theta, \quad du_\beta = 0 \quad \text{along } \beta\text{-lines } \frac{dy}{dz} = -\tan \theta, \quad (3.25)$$

which have the general solution

$$u_\alpha = \alpha + g(\beta), \quad u_\beta = f(\alpha). \quad (3.26)$$

The kinematic boundary conditions in the new variables can be expressed (Wu & Havner 1995, equations (4.10))

$$\left. \begin{array}{l} z = 0 \ (w = 0): \quad \alpha + \beta \cot \theta = 0, \quad u_\alpha + u_\beta \cot \theta = 0, \\ y = 0 \ (v = 0): \quad \alpha = \beta \tan \theta, \quad u_\alpha = u_\beta \tan \theta, \\ y = 1 \ (v = 0): \quad \alpha = \beta \tan \theta + \sec \theta, \quad u_\alpha = u_\beta \tan \theta. \end{array} \right\} \quad (3.27)$$

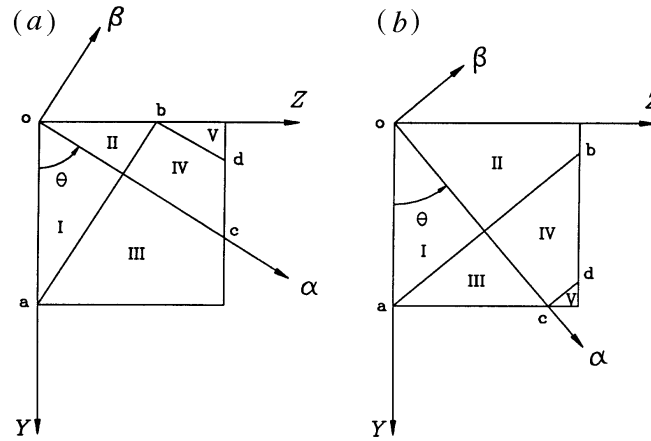


Figure 4. Grain subdivision into regions I through V for kinematic analysis of symmetric bicrystals. (a) $90^\circ > \theta \geq 45^\circ$, (b) $45^\circ \geq \theta > 35.26^\circ$. (Case (a): $9.74^\circ \leq \phi < 35.26^\circ$; $45^\circ \leq \phi < 54.74^\circ$; $54.74^\circ < \phi < 90^\circ$. Case (b): $0 < \phi \leq 9.74^\circ$; $35.26^\circ < \phi \leq 45^\circ$.)

Because of the properties of (3.26) and (3.27), two cases must be considered: (a) $\theta \geq 45^\circ$; and (b) $\theta \leq 45^\circ$. Case (a) includes the following subranges of lattice orientation ϕ (or b): $9.74^\circ \leq \phi < 35.26^\circ$ in range I ($4 + 3\sqrt{2} \geq b > 2$, with $45^\circ \leq \theta < 70.53^\circ$); $45^\circ \leq \phi < 54.74^\circ$ in range II ($\sqrt{2} \geq b > 1$, with $45^\circ \leq \theta < 54.74^\circ$); and $54.74^\circ < \phi < 90^\circ$, range III ($1 > b > 0$, with $54.74^\circ < \theta < 90^\circ$). Case (b) encompasses $0 < \phi \leq 9.74^\circ$ in range I ($b \geq 4 + 3\sqrt{2}$, with $35.26^\circ < \theta \leq 45^\circ$) and $35.26^\circ < \phi \leq 45^\circ$ in range II ($2 > b \geq \sqrt{2}$, with $35.26^\circ < \theta \leq 45^\circ$). In each case, the crystal is divided into five regions, as shown in figure 4. Since the equations expressed in characteristic direction θ are the same for all ranges, the general form of solution obtained in Wu & Havner (1995) for the two cases in range I ($\phi < 35.26^\circ$) applies equally well to range II (which also includes both cases) and range III (corresponding entirely to case (a)).

Let f_i, g_i denote the unknown functions in the i th region (figure 4). The general solutions of (3.26)–(3.27), consistent with continuity of normal velocities across α and β -lines and expressible in terms of a single unknown function f in region I (Wu & Havner 1995, equations (4.11)–(4.15)), are for both cases

$$\left. \begin{aligned} f_1 = f_2 = f(\alpha), \quad g_1 = g_3 = \beta \cot \theta - f(-\beta \cot \theta) \cot \theta, \\ g_2 = g_4 = f(\beta \tan \theta) \tan \theta - \beta \tan \theta, \\ f_3 = f_4 = (\alpha - \cos \theta) \cot \theta \csc^2 \theta - f(\xi) \cot^2 \theta, \\ \xi = \cot^2 \theta (\sec \theta - \alpha) \end{aligned} \right\} \quad (3.28)$$

and, for the separate cases,

$$(a) \quad f_5 = f_3, \quad g_5 = (\beta - \csc \theta) \cot \theta - f(\eta) \cot \theta, \quad \eta = \cot \theta (\csc \theta - \beta), \quad (3.29)$$

$$(b) \quad f_5 = \csc \theta + f(\alpha - \sec \theta), \quad g_5 = g_2. \quad (3.30)$$

The differences in function f among the three ranges are governed by the respective inequalities in the normality constraints (3.17), to which we now turn.

From (2.14) and the equalities in (3.17), the inequalities in those constraints in

terms of the slip rates are simply

$$\left. \begin{aligned} \text{edge AB } (b > 2): \quad \gamma'_3 &\geq 0, \\ \text{edge BC } (2 > b > 1): \quad \gamma'_5 &\geq 0, \\ \text{edge AD } (1 > b > 0): \quad \sqrt{6}/2 &\geq \gamma'_1 \geq 0 \end{aligned} \right\} \quad (3.31)$$

(the first two and very last of which are evident from the slip-systems numbering of yield-locus faces in figure 2). These inequalities can be expressed in terms of d_{yy} , which may be written

$$d_{yy} = \sum (\boldsymbol{\kappa} \cdot \mathbf{b}_j)(\boldsymbol{\kappa} \cdot \mathbf{n}_j)\gamma'_j, \quad \boldsymbol{\kappa} = (1, -1, -b)/\sqrt{b^2 + 2} \quad (3.32)$$

($\boldsymbol{\kappa}$ a unit vector in channel constraint direction Y). Consequently, from (2.14), (3.17), (3.32) and table 1, we obtain

$$\left. \begin{aligned} \text{edges AB and BC } (b > 2, 2 > b > 1): \quad d_{yy} &\leq \frac{b(b-1)}{b^2+2}, \\ \text{edge AD } (1 > b > 0): \quad \frac{b(b-1)}{b^2+2} &\leq d_{yy} \leq \frac{b(b+1)}{b^2+2}. \end{aligned} \right\} \quad (3.33)$$

To express these inequalities in terms of f_i, g_i , observe from (3.26) and standard kinematic relations that

$$d_{\alpha\alpha} = 1, \quad 2d_{\alpha\beta} = f'_i(\alpha) + g'_i(\beta), \quad d_{\beta\beta} = 0 \quad (3.34)$$

in the i th region, with f'_i, g'_i signifying differentiation of these functions with respect to their arguments. Thus, from the coplanar strain-rate transformation between the y, z and α, β axes, there follows (Wu & Havner 1995, equation (4.20))

$$2d_{yy} = 1 + \cos 2\theta - (f'_i + g'_i) \sin 2\theta. \quad (3.35)$$

From (3.5) and (3.8)–(3.9), one has the identities

$$\left. \begin{aligned} \text{edge AB } (b > 2): \quad \sin 2\theta &= \frac{2\sqrt{2}(b+2)(b-1)}{3(b^2+2)}, \quad \cos 2\theta = \frac{b^2-8b-2}{3(b^2+2)}, \\ \text{edges BC and AD } (2 > b > 1, 1 > b > 0): \quad \sin 2\theta &= \frac{2\sqrt{2}b}{b^2+2}, \quad \cos 2\theta = \frac{b^2-2}{b^2+2}. \end{aligned} \right\} \quad (3.36)$$

Therefore, upon substituting (3.35) and (3.36) into (3.33), we obtain the normality constraints governing f_i, g_i :

$$\left. \begin{aligned} b > 2: \quad f'_i + g'_i &\geq -1/\sqrt{2}, \\ 2 > b > 1: \quad f'_i + g'_i &\geq 1/\sqrt{2}, \\ 1 > b > 0: \quad -1/\sqrt{2} &\leq f'_i + g'_i \leq 1/\sqrt{2}. \end{aligned} \right\} \quad (3.37)$$

The final constraints on function f for each range of lattice orientation now can be determined.

For $b > 2$ and $2 > b > 1$, upon substituting (3.28)–(3.30) into (3.37)_{1,2}, we obtain for the regions of figure 4

$$\left. \begin{aligned} \text{I. } f'(\alpha) + f'(-\beta \cot \theta) \cot^2 \theta &\geq k_1 = k_0 - \cot \theta < 0, \\ \text{II. } f'(\alpha) + f'(\beta \tan \theta) \tan^2 \theta &\geq k_2 = k_0 + \tan \theta > 0, \\ \text{III. } f'(\xi) \cot^4 \theta + f'(-\beta \cot \theta) \cot^2 \theta &\geq k_1 - \cot \theta \csc^2 \theta, \\ \text{IV. } f'(\xi) \cot^4 \theta + f'(\beta \tan \theta) \tan^2 \theta &\geq k_2 - \cot \theta \csc^2 \theta, \end{aligned} \right\} \quad (3.38)$$

for both cases (a) and (b) and, in region V,

$$\left. \begin{aligned} \text{V(a). } & f'(\xi) \cot^4 \theta + f'(\eta) \cot^2 \theta \geq k_1 - \cot \theta \csc^2 \theta, \\ \text{V(b). } & f'(\alpha - \sec \theta) + f'(\beta \tan \theta) \tan^2 \theta \geq k_2 \end{aligned} \right\} \quad (3.39)$$

for the separate cases, with

$$\left. \begin{aligned} b > 2: & k_0 = -1/\sqrt{2}, \quad \theta = \tan^{-1} \left\{ \frac{b+2}{\sqrt{2}(b-1)} \right\}, \\ 2 > b > 1: & k_0 = 1/\sqrt{2}, \quad \theta = \tan^{-1}(\sqrt{2}/b). \end{aligned} \right\} \quad (3.40)$$

(i) *Case (a):* $\theta \geq 45^\circ$

In case (a), with $45^\circ \leq \theta < 70.53^\circ$ for $4 + 3\sqrt{2} \geq b > 2$ ($9.74^\circ \leq \phi < 35.26^\circ$) and $45^\circ \leq \theta < 54.74^\circ$ for $\sqrt{2} \geq b > 1$ ($\theta = \phi$), the ranges of the respective arguments of function f in the five regions, as determined from the geometry of figure 4a, are

$$\left. \begin{aligned} \text{I. } & 0 \leq \alpha \leq \cos \theta, \quad 0 \leq -\beta \cot \theta \leq \cos \theta, \\ \text{II(a). } & 0 \leq \alpha \leq \cos \theta, \quad 0 \leq \beta \tan \theta \leq \cos \theta, \\ \text{III(a). } & 0 \leq \cos \theta(1 - \cot \theta) \leq \xi \leq \cos \theta, \quad 0 \leq -\beta \cot \theta \leq \cos \theta, \\ \text{IV(a). } & 0 \leq \cot \theta \csc \theta(1 - \cot \theta) \leq \xi \leq \cos \theta, \quad 0 \leq \beta \tan \theta \leq \cos \theta, \\ \text{V(a). } & 0 < \cot \theta \csc \theta(1 - \cot \theta) + \cos \theta \cot^4 \theta \leq \xi \leq \cos \theta, \\ & 0 < \cot \theta(\csc \theta - \cos \theta) \leq \eta \leq \cos \theta. \end{aligned} \right\} \quad (3.41)$$

Consequently, each of the arguments in (3.38)–(3.39) (case (a)) is encompassed by 0 to $\cos \theta$ for every region. It is seen that, independent of the sign of k_0 , the right-hand sides of (3.38)–(3.39) are negative in regions I, III, and V(a) and positive for all θ only in region II. Thus, one may anticipate that the normality constraint will be critical in region II, although of course region IV must also be investigated. To analyse this constraint the following theorem, easily proved, is needed:

Theorem 3.1. For $p_1 > 0$, $p_2 > 0$, the necessary and sufficient condition that $p_1 F(x) + p_2 F(y) \geq p_3$, where x, y have the same range, is $(p_1 + p_2)F(x) \geq p_3$.

(If the range of y is less than that of x , this condition is sufficient but not necessary.) Applying the theorem to (3.38)₂ we find, for the normality constraint to be satisfied in region II, it is both necessary and sufficient for case (a) that

$$f'(\zeta) \geq k_2 \cos^2 \theta > 0, \quad 0 \leq \zeta \leq \cos \theta \quad (3.42)$$

(as first shown, for range I only, in Wu & Havner (1995, § 4)). This constraint ensures the strict inequality in each of regions I, III and V(a) (making the respective right-hand sides in (3.38)–(3.39) positive). Upon applying (3.42) to region IV, (3.38)₄, one sees it is sufficient for the latter inequality to confirm that $\cot \theta \csc^2 \theta \geq k_2 \cos^2 \theta(1 - \cot^4 \theta)$. From $k_2 = k_0 + \tan \theta$ and (3.40), this reduces to $2\sqrt{2} + \tan \theta > \cot \theta$ in the first range ($b > 2$) and $2\sqrt{2} + \cot \theta$ in the second ($2 > b > 1$), each of which is satisfied by all θ in the respective range. Thus, the normality constraint for case (a) is governed by region II (figure 4a) and reduces to (3.42). Because (3.38)–(3.39) are now strict inequalities in the other four regions, systems 3, 4 ($c\bar{1}, c_2$) for $b > 2$ and systems 5, 6 ($a\bar{3}, b_3$) for $2 > b > 1$ are necessarily active in those regions, but may be inactive in region II. (Systems 1, 2, of course, are active in all regions, from (2.13)₄, since systems 9, 10 are not critical in these two orientation ranges.)

(ii) *Case (b):* $\theta \leq 45^\circ$

In this case, with $35.26^\circ < \theta \leq 45^\circ$ for both $b \geq 4 + 3\sqrt{2}$ ($0 < \phi \leq 9.74^\circ$) and $2 > b \geq \sqrt{2}$ ($35.26^\circ < \phi \leq 45^\circ$), the ranges of the arguments in (3.38)–(3.39) are, from figure 4b,

$$\left. \begin{aligned} \text{I. } & 0 \leq \alpha = \cos \theta, & 0 \leq -\beta \cot \theta \leq \cos \theta; \\ \text{II(b). } & 0 \leq \alpha \leq \cos \theta, & 0 \leq \beta \tan \theta \leq \sin \theta; \\ \text{III(b). } & 0 \leq \xi \leq \cos \theta, & 0 \leq -\beta \cot \theta \leq \cos \theta; \\ \text{IV(b). } & 0 \leq \xi \leq \cos \theta, & 0 \leq \beta \tan \theta \leq \tan \theta (\sec \theta - \sin \theta) \leq \sin \theta; \\ \text{V(b). } & 0 \leq \alpha - \sec \theta \leq \sin \theta (1 - \tan \theta) < \sin \theta, \\ & & 0 \leq \beta \tan \theta \leq \tan \theta \sec \theta (1 - \tan \theta) < \sin \theta. \end{aligned} \right\} \quad (3.43)$$

Because $\sin \theta \leq \cos \theta$ for $\theta \leq 45^\circ$, each range again is encompassed by 0 to $\cos \theta$. However, the ranges for the two parameters in (3.38)₂, region II (which with IV remains the critical one), now are different. Consequently, (3.42) is the required normality constraint throughout the interval $0 \leq \varsigma \leq \sin \theta$ (from the preceding theorem) but may not be necessary in some segment of $\sin \theta \leq \varsigma \leq \cos \theta$.

(c) *Analysis of range III* ($1 > b > 0$)

All of range III corresponds to case (a) (figure 4a), with $54.74^\circ < \theta < 90^\circ$, $\theta = \phi$. Upon substituting (3.28) and (3.29) into the third equation of (3.37), we obtain the following normality constraints in the five regions:

$$\left. \begin{aligned} \text{I. } & k_1 = -1/\sqrt{2} - \cot \theta \leq f'(\alpha) + f'(-\beta \cot \theta) \cot^2 \theta \leq k_3 = 1/\sqrt{2} - \cot \theta, \\ \text{II. } & 0 < k_2 = -1/\sqrt{2} + \tan \theta \leq f'(\alpha) + f'(\beta \tan \theta) \tan^2 \theta \leq k_4 = 1/\sqrt{2} + \tan \theta, \\ \text{III. } & k_1 - \cot \theta \csc^2 \theta \leq f'(\xi) \cot^4 \theta + f'(-\beta \cot \theta) \cot^2 \theta \leq k_3 - \cot \theta \csc^2 \theta, \\ \text{IV. } & k_2 - \cot \theta \csc^2 \theta \leq f'(\xi) \cot^4 \theta + f'(\beta \tan \theta) \tan^2 \theta \leq k_4 - \cot \theta \csc^2 \theta, \\ \text{V. } & k_1 - \cot \theta \csc^2 \theta \leq f'(\xi) \cot^4 \theta + f'(\eta) \cot^2 \theta \leq k_3 - \cot \theta \csc^2 \theta, \\ & \xi = \cot \theta (\csc \theta - \alpha \cot \theta), \quad \eta = \cot \theta (\csc \theta - \beta), \end{aligned} \right\} \quad (3.44)$$

with the ranges of the respective arguments of function f given by (3.41). It is seen that the lower-bound inequalities in (3.44) are exactly the same as the inequalities (3.38)–(3.39) for case (a) of range I ($b > 2$), governed by (3.42). Thus, that constraint also applies to range III. Consequently, upon replacing each f' expression in (3.44) by the greatest lower bound $k_2 \cos^2 \theta$ from (3.42) (which applies throughout the range of every argument in (3.44)), we find that the upper-bound normality constraint is identically satisfied in region II (reducing to $\sqrt{2} > 0$) and that the inequalities in the other regions can be expressed (after extensive trigonometric manipulation):

$$\left. \begin{aligned} \text{I. } & \sqrt{2} \sin 2\theta \leq 1, \\ \text{III., V. } & \sin^2 2\theta + 2\sqrt{2} \sin 2\theta \leq 2, \\ \text{IV. } & 6 \cos^4 2\theta + 5 \cos^2 2\theta - 6 \cos 2\theta \geq 1. \end{aligned} \right\} \quad (3.45)$$

(3.45)₃ (region IV) is satisfied by all θ in range III (requiring only $\theta \geq 49.25^\circ$). From the first constraint of (3.45), however, it is necessary that $\theta \geq 67.5^\circ$; while for the critical regions III and V we must have

$$\sin 2\theta \leq 2 - \sqrt{2}, \quad \text{or} \quad \theta = \phi \geq 72.07^\circ \quad (b \leq 0.4576). \quad (3.46)$$

Therefore, the normality constraints cannot all be satisfied in the subrange $54.75^\circ < \phi < 72.07^\circ$; and we reach the unexpected conclusion that the adopted boundary condition of zero normal velocities along vertical channel walls is too restrictive in this range. Thus, *each crystal will separate from one or both walls along all or part of its length*. (Note that this is consistent with the second equation of (3.16), giving a zero lateral constraint stress in range III.) This subrange will be re-analysed in the next section.

Consider the range $72.07^\circ \leq \phi < 90^\circ$ (no separation) in which (3.44) apply. The theorem in §3*b*(i) (preceding (3.42)) also holds when the signs of its inequalities (but not p_1, p_2) are reversed. Consequently, necessary conditions on f for the right-hand normality constraints in (3.44) to be satisfied are

$$\left. \begin{aligned} \text{I. } f'(\varsigma) &\leq k_3 \sin^2 \theta = \frac{\sqrt{2}(1-b)}{b^2+2}, \quad b = \sqrt{2} \cot \theta; \\ \text{II. } f'(\varsigma) &\leq k_4 \cos^2 \theta = \frac{b(b+2)}{\sqrt{2}(b^2+2)}; \\ \text{III., V. } f'(\varsigma) &\leq k_3 \sin^2 \theta \tan^2 \theta - \tan \theta = \frac{\sqrt{2}(2-4b-b^3)}{b^2(b^2+2)}; \\ \text{IV. } f'(\varsigma) &\leq \frac{k_4 - \cot \theta \csc^2 \theta}{\tan^2 \theta + \cot^4 \theta} = \frac{\sqrt{2}(4+2b-2b^2-b^4)}{b^6+8}, \end{aligned} \right\} \quad (3.47)$$

with ς taking on the full range $(0, \cos \theta)$ in regions I, II (figure 4*a*), but only the ranges of ξ (see (3.41)) as a strictly necessary condition in the other three regions. For $b = \sqrt{6} - 2 = 0.4495$ ($\theta = \phi = 72.37^\circ$), the right-hand sides of (3.47) are identical, equalling 0.3536, while the greatest lower bound on f' (from (3.42)) equals 0.2238. For smaller b (larger ϕ), region II controls; while for larger b (the very narrow range of smaller admissible ϕ), regions III or V control. Therefore, the necessary constraints on f for this part of range III are

$$\begin{aligned} 0 &< \frac{b(2-b)}{\sqrt{2}(b^2+2)} \leq f'(\varsigma) \\ &\leq \left\{ \begin{array}{l} \frac{\sqrt{2}(2-4b-b^3)}{b^2(b^2+2)}, \quad 0.4576 \geq b \geq 0.4495 \quad (72.07^\circ \leq \phi \leq 72.37^\circ), \\ \frac{b(b+2)}{\sqrt{2}(b^2+2)}, \quad 0.4495 \geq b > 0 \quad (72.37^\circ \leq \phi < 90^\circ). \end{array} \right\} \quad (3.48) \end{aligned}$$

The lower bound is identically equal to (3.42) and ς takes on the full range $(0, \cos \theta)$ in the second inequality of (3.48), but not necessarily in the first inequality of (3.48) in case of the right-hand constraint, because of the limited range of parameter ξ in regions III and V (from (3.41)).

To determine which systems necessarily are active in the various regions, we write the equation for γ'_1 in terms of f_i, g_i from (3.32), (3.35), and (2.13)₄ (an intermediate step in the development of range III normality constraints (3.37)₃):

$$\gamma'_1 = \frac{1}{4}\sqrt{6} + \frac{1}{2}\sqrt{3(f'_i + g'_i)}. \quad (3.49)$$

Thus, the lower and upper bounds in (3.44), respectively, correspond to $\gamma'_1 = 0$ and $\gamma'_1 = \frac{1}{2}\sqrt{6}$ (whence $\gamma'_9 = 0$ from (2.13)₄). Consequently, from the preceding analysis of these inequalities, systems 1, 2 (a1, b2) may be inactive only in region II. In addition, for ϕ between 72.07° and 72.37° , systems 9, 10 (a2, b1) may be inactive only in regions

III, V, while for ϕ between 72.37° and 90° these systems may be inactive only in region II (but not, of course, if systems 1, 2 are inactive).

(d) *Crystals separating from channel walls* ($54.74^\circ < \phi < 72.07^\circ$)

In the range of lattice orientations ϕ between 54.74° and 72.07° , the kinematic boundary conditions along $y = 0, 1$ must be modified to reflect merely passive constraint of the rigid channel walls on the respective crystal faces (consistent with zero constraint stress, the second equation of (3.16)). Thus, from (3.27),

$$\left. \begin{aligned} y = 0 \ (v \geq 0) : \quad & \alpha = \beta \tan \theta, \quad u_\alpha \geq u_\beta \tan \theta, \\ y = 1 \ (v \leq 0) : \quad & \alpha = \beta \tan \theta + \sec \theta, \quad u_\alpha \leq u_\beta \tan \theta, \end{aligned} \right\} \quad (3.50)$$

with the inequality necessarily strict along part or all of at least one of the boundaries. Then, from the general solution (3.26) and the continuity of normal velocities across characteristic lines, we obtain

$$\left. \begin{aligned} f_1 = f_2 = f(\alpha), \quad g_1 = g_3 = \beta \cot \theta - f(-\beta \cot \theta) \cot \theta, \\ g_2 = g_4 \geq f(\beta \tan \theta) \tan \theta - \beta \tan \theta, \\ f_3(\alpha) = f_4 = f_5 \geq (\alpha - \cos \theta) \cot \theta \csc^2 \theta - f(\xi) \cot^2 \theta, \\ g_5 \geq f_3(\beta \tan \theta) \tan \theta - \beta \tan \theta, \quad \xi = \cot^2 \theta (\sec \theta - \alpha), \end{aligned} \right\} \quad (3.51)$$

the only differences from the original solutions (3.28)–(3.29) being the inequality signs above.

From the direction of the inequalities in (3.51), the upper bound constraints on function f in (3.44) continue to apply, hence inequalities (3.47) still hold (with the same limitations on the ranges of ζ as before). Let the right-hand sides of these inequalities be denoted c_1, \dots, c_4 for the respective regions. We find $c_3 < c_1 < c_4 < c_2$ in this subrange, with $c_1 = k_2 \cos^2 \theta$ for $\theta = 67.5^\circ$ (recall (3.45)₁), and

$$\left. \begin{aligned} 67.5^\circ < \theta < 72.07^\circ : \quad & c_3 < k_2 \cos^2 \theta < c_1 \quad (2 - \sqrt{2} > b > 0.4576), \\ 54.74^\circ < \theta < 67.5^\circ : \quad & c_1 < k_2 \cos^2 \theta < c_4 \quad (1 > b > 2 - \sqrt{2}) \end{aligned} \right\} \quad (3.52)$$

($k_2 = \tan \theta - 1/\sqrt{2}$). Consequently, in the range between 67.5° and 72.07° , f_3 must be a strict inequality in (3.51) (the crystal separating from the boundary along $y = 1$), while g_2 and g_5 may be taken as equalities. We express f_3 in the form

$$f_3(\alpha) = m_2 \alpha + m_3 - f(\xi) \cot^2 \theta, \quad \xi = \cot^2 \theta (\sec \theta - \alpha), \quad (3.53)$$

with

$$m_2 \alpha + m_3 \geq (\alpha - \cos \theta) \cot \theta \csc^2 \theta, \quad \cos \theta \leq \alpha \leq \sin \theta + \cos \theta \quad (3.54)$$

(from (3.51)). Correspondingly, from the normality constraints (3.37)₃ and the preceding theorem (applied to both directions of constraints), we have, for the regions of figure 4a,

$$\left. \begin{aligned} \text{I.} \quad & -1/\sqrt{2} \leq f'(\zeta) \csc^2 \theta + \cot \theta \leq 1/\sqrt{2}, \\ \text{II.} \quad & -1/\sqrt{2} \leq f'(\zeta) \sec^2 \theta - \tan \theta \leq 1/\sqrt{2}, \\ \text{III.} \quad & -1/\sqrt{2} \leq f'(\zeta) \cot^2 \theta \csc^2 \theta + \cot \theta + m_2 \leq 1/\sqrt{2}, \\ \text{IV.} \quad & -1/\sqrt{2} \leq f'(\zeta) (\tan^2 \theta + \cot^4 \theta) - \tan \theta + m_2 \leq 1/\sqrt{2}, \\ \text{V.} \quad & -1/\sqrt{2} \leq f'(\zeta) \cot^2 \theta \csc^2 \theta - \tan \theta + m_2 \sec^2 \theta \leq 1/\sqrt{2}. \end{aligned} \right\} \quad (3.55)$$

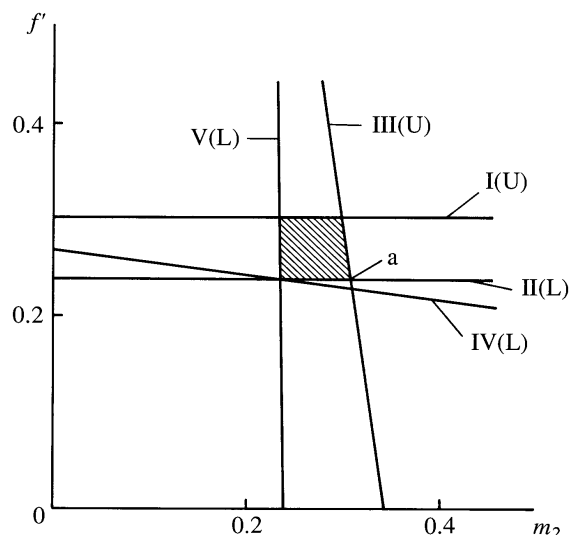


Figure 5. Governing upper (U) and lower (L) bound normality constraints and solutions domain (shaded area) in f' , m_2 space, evaluated for $\theta = \phi = 70^\circ$. (Point 'a' corresponds to equations (3.58).)

For $\theta = 67.5^\circ$, the first upper bound and the second lower bound give $f' = \frac{1}{4}$, while the third upper bound and the fifth lower bound give $m_2 = 0.24264$, both uniquely, with all other inequalities satisfied (the lower bound (3.55)₄ also being an equality). This combination of constraints also governs f' and m_2 throughout the subrange $67.5^\circ < \theta < 72.07^\circ$. Thus, sufficient constraints on f' may be expressed:

$$(\tan \theta - 1/\sqrt{2}) \cos^2 \theta \leq f'(\zeta) \leq (1/\sqrt{2} - \cot \theta) \sin^2 \theta, \quad 67.5^\circ \leq \theta \leq 72.07^\circ \quad (3.56)$$

(the lower bound identically $k_2 \cos^2 \theta$, as before), with m_2 constrained by the respective upper and lower bounds III, V for an f' satisfying (3.56) (and both the fourth and fifth lower bounds in (3.55) intersecting $f' = k_2 \cos^2 \theta$ at the point $m_2 = f'(1 - \cot^4 \theta)$). These four inequalities define a region of admissible solutions in f' , m_2 space (reducing to a point at $\theta = 67.5^\circ$, as noted) which is shown evaluated for $\theta = \phi = 70^\circ$ in figure 5. In Wu (1995), the largest m_2 consistent with the full range of possible f' values from (3.56) is chosen. As evident from figure 5, this is determined by the intersection of the upper bounds for regions I and III in (3.55). The result is

$$m_2 = (1/\sqrt{2} - \cot \theta)(1 - \cot^2 \theta) = (\sqrt{2}/4)(1 - b)(2 - b^2). \quad (3.57)$$

(At $\theta = 70^\circ$, this gives 0.2977, whereas the corresponding term in f_3 , with no boundary separation, $\cot \theta \csc^2 \theta$ from (3.28)₄, equals 0.4122.) Alternatively, choosing the absolute largest m_2 will give a smaller boundary separation along $y = 1$ than (3.57). In this case, from the lower bound (3.55)₂ (or (3.56)) and the upper bound (3.55)₃, we have

$$f' = (\tan \theta - 1/\sqrt{2}) \cos^2 \theta, \quad m_2 = (1/\sqrt{2})(1 + \cot^4 \theta) - \cot \theta \csc^2 \theta. \quad (3.58)$$

(For $\theta = 70^\circ$ (figure 5), these give $f' = 0.2387$ and $m_2 = 0.3073$.)

The quantity m_3 is now determined from (3.54)₁. To minimize boundary separation, we choose the smallest value consistent with that inequality, which must be evaluated at the maximum α corresponding to the lower-right hand corner of the

crystal, whence

$$m_3 = \cot \theta \csc \theta - m_2(\sin \theta + \cos \theta), \quad (3.59)$$

with m_2 given by (3.57) or (3.58)₂. (At $\theta = 70^\circ$, the respective values are 0.00579 and -0.00658 versus $-\cot^2 \theta \csc \theta = -0.1410$ from (3.28)₄ for no boundary separation.)

For $54.74^\circ < \theta < 67.5^\circ$ ($1 > b > 2 - \sqrt{2}$), g_2 and g_5 , as well as f_3 , must be inequalities in (3.51) (from (3.52)₂) and the crystal will separate from the boundary along both walls. The previous equation (3.53) for f_3 still pertains, while g_2 and g_5 now are taken as

$$\left. \begin{aligned} g_2(\beta) &= f(\beta \tan \theta) \tan \theta - m_1 \beta, & m_1 &\leq \tan \theta, \\ g_5(\beta) &= f_3(\beta \tan \theta) \tan \theta - m_1 \beta \\ &= m_2 \beta \tan^2 \theta + m_3 \tan \theta - f(\eta) \cot \theta - m_1 \beta, & \eta &= \cot \theta (\csc \theta - \beta), \end{aligned} \right\} \quad (3.60)$$

the inequality on m_1 corresponding to the necessary condition $v > 0$ along $y = 0$. (We did not investigate the possibility of choosing a different parameter, m_4 say, for region V.) The inequalities in (3.55) for regions I and III are unchanged, while the others become

$$\left. \begin{aligned} \text{II.} & \quad -1/\sqrt{2} \leq f'(\zeta) \sec^2 \theta - m_1 \leq 1/\sqrt{2}, \\ \text{IV.} & \quad -1/\sqrt{2} \leq f'(\zeta) (\tan^2 \theta + \cot^4 \theta) - m_1 + m_2 \leq 1/\sqrt{2}, \\ \text{V.} & \quad -1/\sqrt{2} \leq f'(\zeta) \cot^2 \theta \csc^2 \theta - m_1 + m_2 \sec^2 \theta \leq 1/\sqrt{2}. \end{aligned} \right\} \quad (3.61)$$

To minimize boundary separation along $y = 0$, which seems to us physically reasonable, we set m_1 equal to its maximum value, determined from the respective upper and lower bounds (3.55)₁ and (3.61)₁, regions I and II:

$$m_1 = (1/\sqrt{2}) \sec^2 \theta - \tan \theta = \frac{b^2 - 2b + 2}{\sqrt{2}b^2}. \quad (3.62)$$

(This equals $\tan \theta$ at $\theta = 67.5^\circ$, as required.) Then, since these two bounds now are equal, we have

$$f' = (1/\sqrt{2} - \cot \theta) \sin^2 \theta, \quad 54.74^\circ < \theta \leq 67.5^\circ \quad (1 > b \geq 2 - \sqrt{2}). \quad (3.63)$$

Upon substituting (3.62)–(3.63) into the remaining inequalities, we find that upper bound (3.55)₃, region III, and lower bounds (3.61)_{2,3}, regions IV and V, control m_2 and are equal as well. Consequently, m_2 is uniquely given by (3.57), with m_3 again determined from (3.59). (In other words, the choice of m_1 that minimizes boundary separation along $y = 0$, for all $\theta = \phi$ between 54.74° and 67.5° , causes the governing normality constraints corresponding to upper bounds in regions I and III and lower bounds in regions II, IV and V (figure 4a) to intersect at a single point in f', m_2 space, given by (3.57) and (3.63).)

Because the lower-bound normality constraints in regions I and III, and the upper-bound constraints in regions II, IV and V, are strict inequalities from (3.55) and (3.61), for all ϕ between 54.74° and 72.07° , slip systems 1, 2 must be active in the former regions and systems 9, 10 in the latter (recall (3.49)). Moreover, in the range $67.5^\circ < \phi < 72.07^\circ$, with m_2 given by (3.57) and f' lying between its bounds in (3.56), both system pairs are active in all five regions.

Finally, from (3.26), (3.51), (3.53), (3.59) and (3.60), the normal velocity $v =$

$u_\alpha \cos \theta - u_\beta \sin \theta$ along $y = 0, 1$ is determined as

$$\left. \begin{aligned} y = 0: \quad v &= z(\tan \theta - m_1) \cos^2 \theta \geq 0 \quad (54.74^\circ < \theta \leq 67.5^\circ \text{ only}), \\ y = 1: \quad v &= (1 - z)(m_2 \sin^2 \theta - \cot \theta) \leq 0, \end{aligned} \right\} \quad (3.64)$$

with m_1, m_2 given by (3.62) and (3.57) or (3.58)₂, respectively. Thus, only the lower right-hand edge ($y = 1, z = 1$) of the crystal remains in contact with the wall along that face; while only the interface edge ($y = 0, z = 0$) remains in contact for the range of separation (ϕ between 54.74° and 67.5°) of the other vertical face.

(e) *Tangential velocity discontinuities*

Let $[q]_{i,j}$ denote the difference $q_i - q_j$ in value of a variable q between regions i, j at their common boundary. When there is no separation of the crystal from channel walls (orientation ranges I, II and part of III), the possible tangential velocity differences along interior boundaries of the five regions (figure 4) are, from (3.26) and (3.28)–(3.30),

$$[u_\alpha]_{I,II} = [u_\alpha]_{III,IV} = -f(0) \sec \theta \csc \theta, \quad [u_\beta]_{I,III} = [u_\beta]_{II,IV} = f(\cos \theta) \csc^2 \theta, \quad (3.65)$$

for both cases (a) ($\theta \geq 45^\circ$) and (b) ($\theta \leq 45^\circ$), and

$$\left. \begin{aligned} \text{(a)} \quad [u_\alpha]_{IV,V} &= f(\cos \theta) \sec \theta \csc \theta = \tan \theta [u_\beta]_{I,III}, \\ \text{(b)} \quad [u_\beta]_{IV,V} &= -f(0) \csc^2 \theta = \cot \theta [u_\alpha]_{I,II} \end{aligned} \right\} \quad (3.66)$$

for the separate cases (as first given in Wu & Havner (1995, equations (5.1)–(5.2))). Because for case (a) $f(\zeta)$ is monotonely increasing throughout the range $(0, \cos \theta)$ from (3.42), $f(0)$ and $f(\cos \theta)$ cannot both be zero. Thus, there will be tangential velocity discontinuities along lines ab and bd, or line oc (figure 4a), or both.

For case (b), inequality (3.42) necessarily holds only in the range $(0, \sin \theta)$ and it is conceivable that $f'(\zeta)$ may be negative in part of the range $\sin \theta < \zeta \leq \cos \theta$. However, as proved in Wu & Havner (1995, §5), using the mean value theorem, it is still impossible for both $f(0)$ and $f(\cos \theta)$ to be zero, and there will be tangential velocity discontinuities as in case (a) (but with line cd (figure 4b), replacing bd).

Consider now the subrange $54.74^\circ < \phi < 72.07^\circ$ (case (a)), in which crystals separate from channel walls. From (3.26), (3.51), (3.53) and (3.60), with m_3 given by (3.59) to minimize boundary separation, the possible tangential velocity differences along interior region boundaries are

$$\left. \begin{aligned} [u_\alpha]_{I,II} &= [u_\alpha]_{III,IV} = -f(0) \sec \theta \csc \theta, \\ [u_\beta]_{I,III} &= [u_\beta]_{II,IV} = f(\cos \theta) \csc^2 \theta + m_2 \sin \theta - \cot \theta \csc \theta, \\ [u_\beta]_{IV,V} &= f(\cos \theta) \sec \theta \csc \theta + m_2 \sin \theta \tan \theta - \csc \theta = \tan \theta [u_\beta]_{I,III} \end{aligned} \right\} \quad (3.67)$$

The necessary and sufficient conditions for there to be no tangential velocity discontinuities obviously are $f(0) = 0$, $f(\cos \theta) = \cos \theta - m_2 \sin^3 \theta$, with $f'(\zeta)$ constrained by (3.56). From the mean value theorem, $f'(\zeta)$ must equal the slope \bar{f}' of the line connecting $(0, 0)$ and $(\cos \theta, f(\cos \theta))$ at one or more points in the interval. For m_2 given by (3.57) (which may be adopted throughout the subrange) and the foregoing values $f(0), f(\cos \theta)$, this slope would be

$$\bar{f}' = (2 + \sqrt{2} \cot 2\theta) \sin^2 \theta = \frac{b^2 + 4b - 2}{b(b^2 + 2)}. \quad (3.68)$$

Upon comparing (3.68) with the bounds (3.56) on f' for $\theta = \phi$ between 67.5° and 72.07° (separation along $y = 1$), we find that the slope falls within the admissible range only if $69.79^\circ \leq \phi \leq 70.40^\circ$ ($0.5205 \geq b \geq 0.5037$).

For ϕ between 54.74° and 67.5° (necessary separation along both boundaries), (3.68) does not equal the uniform f' value given by (3.63) corresponding to minimum separation in this range. Nor does a slope f' calculated with m_2 given by (3.58)₂ (minimum boundary separation for $67.5^\circ \leq \phi < 72.07^\circ$) equal the associated uniform f' value from (3.58)₁. Thus, the only possibility for there to be no tangential velocity discontinuities is in the narrow orientation range $69.79^\circ \leq \phi \leq 70.40^\circ$, with m_2 given by (3.57), $f'(\varsigma)$ constrained by (3.56) and its mean value given by (3.68) (and, of course, $f(0) = 0$). (At $\phi = 70^\circ$ (figure 5), for example, $f'(\varsigma)$ may range between 0.2387 and 0.3030, but its mean value must be 0.2778 for all $[u_\beta]$ at interior boundaries to be zero.)

(f) *Initiation of subgrains: the basic solution*

We now turn to the determination of initial lattice-rotation rates within the bicrystal. From (2.10)₂, (2.12), (2.13) and figure 2, the components on lattice axes of the axial vector \mathbf{a}_Ω of plastic spin Ω are

$$\left. \begin{aligned} b > 2 \text{ (edge AB): } & a_1 = a_2 = \frac{1}{4} - (\frac{1}{4}\sqrt{6})\gamma'_3, \\ 2 > b > 1 \text{ (edge BC): } & a_1 = a_2 = \frac{1}{4} + (1/\sqrt{6})\gamma'_5, \\ 1 > b > 0 \text{ (edge AD): } & a_1 = a_2 = -\frac{1}{4} + (1/\sqrt{6})\gamma'_1 \end{aligned} \right\} \quad (3.69)$$

(with $a_3 = 0$, since the lattice is rotating in the YZ plane). We find for the respective edges of the yield-locus face (from (2.13), table 1, (3.32) and (3.35)):

$$\left. \begin{aligned} \text{edge AB: } & \gamma'_3 = 1/\sqrt{6} + (1/\sqrt{3})(f'_i + g'_i), \\ \text{edge BC: } & \gamma'_5 = -\frac{1}{4}\sqrt{6} + (\frac{1}{2}\sqrt{3})(f'_i + g'_i), \\ \text{edge AD: } & \gamma'_1 = \frac{1}{4}\sqrt{6} + (\frac{1}{2}\sqrt{3})(f'_i + g'_i). \end{aligned} \right\} \quad (3.70)$$

Thus, from $a_x = \sqrt{2}a_1$ (the second equation of (2.12)) and (3.69)–(3.70), the plastic spin about the loading axis in the i th region for the respective ranges of b (or ϕ) is

$$\left. \begin{aligned} b > 2 \text{ (} 0 < \phi < 35.26^\circ \text{): } & a_x = -\frac{1}{2}(f'_i + g'_i), \\ 2 > b > 1 \text{ (} 35.26^\circ < \phi < 54.74^\circ \text{), } & \\ 1 > b > 0 \text{ (} 54.74^\circ < \phi < 90^\circ \text{): } & a_x = \frac{1}{2}(f'_i + g'_i). \end{aligned} \right\} \quad (3.71)$$

The lattice spin ϕ'_i in the i th region is given by the basic kinematic relation

$$\phi'_i \equiv \omega_x = w_x - a_x, \quad (3.72)$$

where (from (3.26))

$$w_x = W_{zy} = W_{\beta\alpha} = \frac{1}{2} \left(\frac{\partial u_\beta}{\partial \alpha} - \frac{\partial u_\alpha}{\partial \beta} \right) = \frac{1}{2}(f'_i - g'_i) \quad (3.73)$$

(Wu & Havner 1995, equation (6.6)). Therefore, from (3.71)–(3.73), we have the following general results for initial lattice-rotation rate in (110) channel die compression:

$$\left. \begin{aligned} b > 2: & \phi'_i = f'_i(\alpha), \\ 2 > b > 1, \quad 1 > b > 0: & \phi'_i = -g'_i(\beta). \end{aligned} \right\} \quad (3.74)$$

Because each function f_i , g_i is linearly related to $f(\zeta)$ in every orientation range and is otherwise linear (recall (3.28)–(3.30), (3.51), (3.53) and (3.60)), it is evident from (3.74) that choosing $f(\zeta)$ to be a linear function will result in a *uniform rate of initial lattice rotation within each region* (figure 4), as was pointed out for range I in Wu & Havner (1995, §6). Such local uniformity seems to us physically likely as well as necessary if lattice structure and orientation are to retain their meaning over finite regions. Thus, for all orientation ranges, we take $f(\zeta)$ in the form

$$f(\zeta) = c(\phi)\zeta + d(\phi), \quad (3.75)$$

which we shall call the ‘basic solution’.

In range III, (3.75) is made consistent with (3.63) (minimum boundary separation, ϕ between 54.74° and 67.5°) and with (3.68) (no tangential velocity discontinuities, ϕ between 69.79° and 70.40°) by setting c equal to the respective f' in each subrange. Moreover, (3.68) equals the *upper* bound in (3.56) (applicable to $67.5^\circ \leq \phi \leq 72.07^\circ$ and identically (3.63)) at $\phi = 69.79^\circ$ and the *lower* bound in (3.56) at $\phi = 70.40^\circ$ (which bound applies to the same range and also equals the lower bound in (3.48), applicable to $72.07^\circ \leq \phi < 90^\circ$). Therefore, following Wu (1995), we set c equal to these upper and lower limits on f' in (3.56), for $67.5^\circ \leq \phi \leq 69.79^\circ$ and $70.40^\circ \leq \phi < 90^\circ$, respectively, to provide smooth transitions for function f between all subranges (both with and without boundary separation) in range III.

For each of ranges I and II, which have only lower bound constraints on f' from (3.42), we equate c to the respective bound (recall from (3.38)₂ and (3.40) that k_2 is different for the two ranges). This will minimize the intensity of tangential velocity discontinuities along abd in relation to oc in figure 4*a* and along ab in relation to ocd in figure 4*b*. (These relative discontinuities also are minimized by the foregoing choices for c in range III.) Also, since (3.42) is now an equality in region II, systems 3, 4 in range I ($b > 2$) and systems 5, 6 in range II ($2 > b > 1$) are not active in this region. Thus, the choice of the smallest $f(\zeta)$ satisfying all normality constraints is equivalent to the perspective (as remarked in Wu & Havner (1995, §6)) ‘that if the kinematic and normality conditions do not require a critical slip system to be active in a particular region, it will not be.’

To summarize, the orientation dependence of parameter c in the basic solution (3.75) for ranges I, II and III may be taken as follows (Wu 1995, equations (4.109)):

$$\left. \begin{array}{l} \text{I.} \quad 0 < \phi < 35.26^\circ \quad (b > 2): \\ \quad \quad \quad \theta = \phi + 35.26^\circ, \quad c = (\tan \theta - 1/\sqrt{2}) \cos^2 \theta, \\ \text{II.} \quad 35.26^\circ < \phi < 54.74^\circ \quad (2 > b > 1): \\ \quad \quad \quad \theta = \phi, \quad c = (\tan \theta + 1/\sqrt{2}) \cos^2 \theta, \\ \text{III.} \quad \left\{ \begin{array}{l} 54.74^\circ < \phi \leq 69.79^\circ \quad (1 > b \geq 0.5205): \\ \quad \quad \quad \theta = \phi, \quad c = (1/\sqrt{2} - \cot \theta) \sin^2 \theta, \\ 69.79^\circ \leq \phi \leq 70.40^\circ \quad (0.5205 \geq b \geq 0.5037): \\ \quad \quad \quad \theta = \phi, \quad c = (2 + \sqrt{2} \cot 2\theta) \sin^2 \theta, \\ 70.40^\circ \leq \phi < 90^\circ \quad (0.5037 \geq b > 0): \\ \quad \quad \quad \theta = \phi, \quad c = (\tan \theta - 1/\sqrt{2}) \cos^2 \theta. \end{array} \right\} \end{array} \right\} \quad (3.76)$$

(Note that c is not continuous across the singular orientations $\phi = 35.26^\circ$ ($b = 2$) and $\phi = 54.74^\circ$ ($b = 1$), which, respectively, correspond to vertex B and a line connecting vertex C with the midpoint of edge AD of the yield locus, figure 2.) Parameter

Table 2. Parameters c , m_1 , m_2 for continuity of f_i , g_i between subrange boundaries in range III

subrange	$54.74^\circ < \theta \leq 67.5^\circ$	$67.5^\circ \leq \theta \leq 72.07^\circ$	$72.07^\circ \leq \theta < 90^\circ$
c	$(1/\sqrt{2} - \cot \theta) \sin^2 \theta$	$(\tan \theta - 1/\sqrt{2}) \cos^2 \theta$	$(\tan \theta - 1/\sqrt{2}) \cos^2 \theta$
m_1	$(1/\sqrt{2}) \sec^2 \theta - \tan \theta$	$\tan \theta$	$\tan \theta$
m_2	$(1/\sqrt{2} - \cot \theta)(1 - \cot^2 \theta)$	$(1/\sqrt{2})(1 + \cot^4 \theta) - \cot \theta \csc^2 \theta$	$\cot \theta \csc^2 \theta$

$d = f(0)$ remains arbitrary at present, but must be chosen as zero in the subrange $69.79^\circ \leq \phi \leq 70.40^\circ$ for there to be no tangential velocity discontinuities (as seen in §3e).

Although (3.76) permits continuity of $f(\zeta)$ within range III, the corresponding equation (3.57) for m_2 has a small discontinuity with $\cot \theta \csc^2 \theta$ (compare (3.28)₄ and (3.53) for f_3) at $\theta = 72.07^\circ$, the transition orientation between boundary separation and no separation along $y = 1$. (The respective values are 0.3434 and 0.3574.) Thus, there also are discontinuities in m_3 (from (3.59)) and in $f_3 = f_4 = f_5$ and g_5 (from (3.51) and (3.53)). All function discontinuities are eliminated within range III if we make the alternative choice (3.58) for f' and m_2 , θ between 67.5° and 72.07° (and, of course, also take $d(\phi)$ to be continuous). With f_3 and g_2 , g_5 expressed in the respective forms (3.53) and (3.60) throughout the range, the complete set of *continuous* parameters c , m_1 and m_2 may be written as shown in table 2. The respective subranges (in order) correspond to double boundary separation, single separation and no separation. (There now will be tangential velocity discontinuities throughout range III.)

Upon substituting the basic solution (3.75) and the relevant ones of equations (3.28)–(3.30), (3.51), (3.53), (3.60) and (3.62) into (3.74), we obtain a complete set of equations for the initial lattice-rotation rates ϕ'_i in the various regions (figure 4) and ranges:

$$\left. \begin{aligned}
 \text{I.} \quad b > 2: \quad & \phi'_1 = \phi'_2 = c > 0, \\
 & \phi'_3 = \phi'_4 = \cot \theta (\csc^2 \theta + c \cot^3 \theta) > 0, \\
 & \text{case (a) } \phi'_5 = \phi'_3, \quad \text{case (b) } \phi'_5 = \phi'_1, \\
 \text{II.} \quad 2 > b > 1: \quad & \phi'_1 = \phi'_3 = -\cot \theta (1 + c \cot \theta) < 0, \\
 & \phi'_2 = \phi'_4 = \tan \theta (1 - c \tan \theta) > 0, \\
 & \text{case (a) } \phi'_5 = \phi'_1, \quad \text{case (b) } \phi'_5 = \phi'_2, \\
 \text{III.} \quad 1 > b > 0: \quad & \phi'_1 = \phi'_3 = -\cot \theta (1 + c \cot \theta) < 0, \\
 & \phi'_2 = \phi'_4 = m_1 - c \tan^2 \theta > 0, \\
 & \phi'_5 = m_1 - m_2 \tan^2 \theta - c \cot^2 \theta.
 \end{aligned} \right\} \quad (3.77)$$

In range III, m_1 is given by table 2; and m_2 is given by table 2, or by (3.57) for θ between 67.5° and 72.07° ($2 - \sqrt{2} \geq b > 0.4576$) and by table 2 in the rest of the range. In ranges I and II, c is given by (3.76); and in range III it is given either by table 2 or (3.76) (consistent with m_2).

It is seen from equations (3.77) that in range I, case (a), the crystal initially begins to form two subgrains (because of the finitely differing rates of lattice rotation) consisting of regions I and II, and regions III, IV and V (figure 4a); while for case (b), (figure 4b), another subgrain is initiated in region V (since there the crystal

lattice is rotating at the same rate as in regions I and II). However, the shearing strain-rate $d_{\alpha\beta}$ differs among all five regions, from the second equation of (3.34) and (3.28)–(3.30); hence, each region may be expected to form a subgrain as deformation proceeds (and to subdivide further, as will be discussed in §5).

The counterclockwise rotation of the lattice in all regions in range I is qualitatively consistent with the counterclockwise, uniform lattice rotation of single crystals in (110) channel die compression in this range (see Havner 1992, §5.5). Moreover, the initiating subgrain I–II adjacent to the symmetry plane has much the smaller lattice-rotation rate, which seems physically likely since the shearing of this part of the crystal is constrained by the symmetry interface. As a numerical example, consider the range I orientation $\phi = 9.736^\circ$, $\theta = 45^\circ$, the transition between cases (a) and (b). From (3.76) and (3.77), we find $\phi'_1 = 0.1464$, $\phi'_3 = 2.1464$ (radians per unit logarithmic compressive strain e_L). In contrast, for a single crystal in this orientation, from equation (3.12) in Fuh & Havner (1989), one obtains $\phi' = \omega_x = 1.0$ (obviously close to the average of the initial subgrain rates). However, in neither the single crystal nor the bicrystal case may these (initial) rotation rates be thought of as constant. For the former, both minimum plastic spin (Fuh & Havner 1989) and several different hardening rules (Havner & Chidambarrao 1987) predict the same (uniform) finite deformation and lattice rotation, up to the high-symmetry orientation $Y = [1\bar{1}\bar{2}]$, from any initial lattice orientation in range I. The exact theoretical result for the logarithmic compressive strain at which the lattice has rotated 25.53° (0.4456 rad) from $\phi = 9.736^\circ$ to $Y = [1\bar{1}\bar{2}]$ is $e_L = 0.7520$ (from Fuh & Havner 1989, equation (3.19)). Rotation at this strain for an assumed constant rate of 1.0 would be 0.752 rad, of course, or approximately 70% larger than the correct result. In the bicrystal, because of the non-uniformity, the present analysis at the yield point cannot predict the amounts of lattice rotation after a finite strain. That very difficult problem awaits analytical investigation. Analogous to the single crystal case, however, it seems to us a certainty that those rotations would be considerably less than indicated by simple extrapolation using the initial rates.

Tangential velocity discontinuities along lines oc and (case (a) only) bd (figure 4), correspond in range I ($\theta = \phi + 35.26^\circ$) to intersections with the crystal surface of slip plane $(1\bar{1}\bar{1})$ common to systems 3, 4. A tangential velocity discontinuity along line ab between initiating subgrains in range I does not correspond to a crystallographic slip plane, however, nor do any tangential velocity–discontinuity lines in ranges II and III ($\theta = \phi$). We interpret the formation of all tangential velocity discontinuities at the (fully plastic) yield point as marking the initiation of shear bands, whether or not these lines lie along crystallographic slip planes.

In range II, case (b), in contrast to range I, regions I and III, and II, IV and V begin to form subgrains (from (3.77)) separated by line oc, with ab and cd representing the initiation of shear bands across grains. However, as previously remarked for range I, $d_{\alpha\beta}$ differs among regions and we expect subgrains to be initiated in every region as deformation proceeds. For case (a), region V begins to form a separate subregion at the yield point, according to (3.77); and bd represents the initiation of another shear band between subgrains. The initiating subgrain I–III adjacent to the bicrystal interface has a clockwise lattice-rotation rate, while in regions II and IV the lattice is rotating counterclockwise. Opposing rotation rates within each crystal are not surprising since the lattice is stable in single crystals uniformly shearing in this range (see Fuh & Havner 1989, §3.1, for example). However, the predicted values for any orientation in range II ($35.26^\circ < \phi < 54.74^\circ$) seem problematic because the

clockwise rate adjacent to the interface is an order of magnitude greater than the counterclockwise rate in regions II and IV away from the interface. (Other numerical difficulties in interpreting the analytical solution in this range are noted near the end of § 4, with further discussion in § 5.)

In range III, interpretations are as in range II, case (a), with two notable exceptions. For $b > 0.4576$ ($\phi < 72.07^\circ$), corresponding to which the bicrystal begins to separate from one or both boundaries (as we have seen), the lattice-rotation rate in region V differs from that in each of regions I and II. Furthermore, the rates seem to us much more plausible than in range II, with initiation of subgrain I–III adjacent to the interface marked by a much smaller clockwise lattice-rotation rate than the counterclockwise one in (initiating) subgrain II–IV. (As an example, for $\phi = \theta = 70^\circ$, equations (3.77) and table 2 give $\phi'_1 = -0.3956$, $\phi'_2 = 0.9458$ and $\phi'_5 = 0.3959$.) In every range, the initiating grain subdivisions and lattice-rotation rates in the left-hand crystal B (figure 1), are mirror images of those in right-hand crystal A.

4. Comparison with elastoplastic finite element solutions

In the following, selected results from finite element analyses of the elastoplastic transition for several different crystal orientations are presented and compared with stress states and velocity fields from the rigid–plastic analytical solutions. Small strain theory has been adopted in the elastoplastic analysis; hence any changes in crystal configuration during the transition from purely elastic to fully plastic response are taken as negligible. From considerations of length, we omit the equations of the finite element crystal model, for which see Wu (1995, ch. 2 and 5). (The model is similar to other rate-independent finite element crystal models in the literature, the earliest one of which apparently is that of Havner (1971), with Hu *et al.* (1993) a recent example.)

(a) Finite element model

An elastoplastic, incremental stiffness matrix corresponding to cubic elastic anisotropy and the most general crystal slip-system kinematics (12 potentially active systems) is derived in Wu (1995, § 2.2). For comparison with rigid–plastic analyses of the yield-point state, the hardening matrix therein is set equal to zero; hence slip-systems hardening is disregarded during the elastoplastic transition (recall the discussion following (2.8)). An aluminium bicrystal is chosen for evaluation, with all finite element calculations made using the elastic compliances given in Nye (1957, table 10): $s_{11} = 1.59$, $s_{12} = 0.58$, $s_{44} = 3.52$ (units 10^{-2} (GPa) $^{-1}$). The critical shear strength τ_0 is taken to be 13 MPa.

To confirm numerically that the spatial non-uniformity in the bicrystal is only two dimensional, a 16-node, displacement-based, three-dimensional isoparametric element was chosen, with each grain subdivided into eight elements (two along each edge). For $\phi = 9.74^\circ$ ($\theta = 45^\circ$ in figure 4) and other orientations calculated, it was found (Wu 1995, § 5.2) that the distributions of stress and strain increments are independent of loading direction X and that σ_{xy} and σ_{xz} are zero throughout the elastoplastic transition. Consequently, the resolved shear stresses have the pairwise symmetries expressed in (2.8) and the yield locus is as shown in figure 2. It also was found that the stress state of every material point undergoing elastoplastic (as distinct from purely elastic) response lies on the face ABCD, as we concluded would be the case for the rigid–plastic model in Wu & Havner (1995, § 3).

Wu (1995, § 5.2) numerically investigated all possible elastoplastic stiffness matrices for face ABCD (figure 2). He found that the matrix is non-singular and has the same form as the elastic stiffness matrix for all interior points (only systems 1, 2 critical) and edges AB (systems 1, 2, 3, 4), BC (systems 1, 2, 5, 6) and AD (systems 1, 2, 9, 10), but that it is singular for edge CD (systems 1, 2, 7, 8) and the six or eight-fold vertices A, B, C, D.

Based upon the demonstrated two-dimensional character of the problem, a reduced incremental stiffness matrix corresponding to the yield locus and slip-system kinematics of § 2 has been adopted for incorporation into an 8-node, two-dimensional isoparametric element (Wu 1995, § 5.3). From a convergence study of the numerical yield-point load for lattice orientation $\phi = 9.74^\circ$, using uniform $n \times n$ finite element grids in the right-hand crystal, it was found (Wu 1995, figure 8) that the compressive force for a 10×10 grid is barely distinguishable throughout the elastoplastic transition from that for an 8×8 grid. Moreover, the yield-point load for the 10×10 grid is only 0.05% smaller than f_0 given by (3.14) for this orientation ($f_0 = 4.42\tau_0$), which is the same as the single crystal yield-point load (see Havner 1992, § 5.4)† because of the uniformity of the stress state in the rigid–plastic crystal. Consequently, a 10×10 grid (100 elements) has been adopted for the two-dimensional finite element calculations.

For subsequent comparisons, we define two dimensionless parameters which are measures of the closeness of numerical (finite element) and analytical (rigid–plastic) results. These are:

$$r_1 = \frac{\sum\{(v_i - v_i^*)^2 + (w_i - w_i^*)^2\}}{\sum\{(v_i^*)^2 + (w_i^*)^2\}}, \quad (4.1)$$

in which v_i , w_i and v_i^* , w_i^* are, respectively, the analytical and final finite element velocities at a nodal point; and

$$r_2 = f^*/f_0, \quad (4.2)$$

where f_0 is the analytical yield-point load (from (3.14)–(3.16)) and f^* is the converged limit load of the finite element calculations. Finally, we introduce a third dimensionless parameter that is a measure of the closeness of the (elastoplastic) finite element results to rigid–plastic response at the end of the calculations for a given orientation:

$$r_3 = \frac{\sum(d\varepsilon_p^2)}{\sum(d\varepsilon^2)}, \quad (4.3)$$

where the sums are made over all integration points within elements, and $d\varepsilon^2$ and $d\varepsilon_p^2$ represent, respectively, the sum of squares of tensorial components of the total and plastic strain increments in the final calculation step. Ideally, $r_1 \rightarrow 0$, $r_2 \rightarrow 1$ and $r_3 \rightarrow 1$.

(b) Comparisons of analytical and numerical results

In Wu (1995, § 5.4), comparisons between analytical and finite element results are made for each of five lattice orientations: $\phi = 9.74^\circ$, 45° , 60° , 70° and 80° . The first and second respectively belong to ranges I ($b > 2$) and II ($2 > b > 1$), while the others belong to the three subranges (table 2) of range III ($1 > b > 0$). Here we

† In a single aluminium crystal, the exact *elastic limit* load for $\phi = 9.74^\circ$ is $f_E = 3.56\tau_0$ from table 2, (5.11) and (5.38) in Havner (1992).

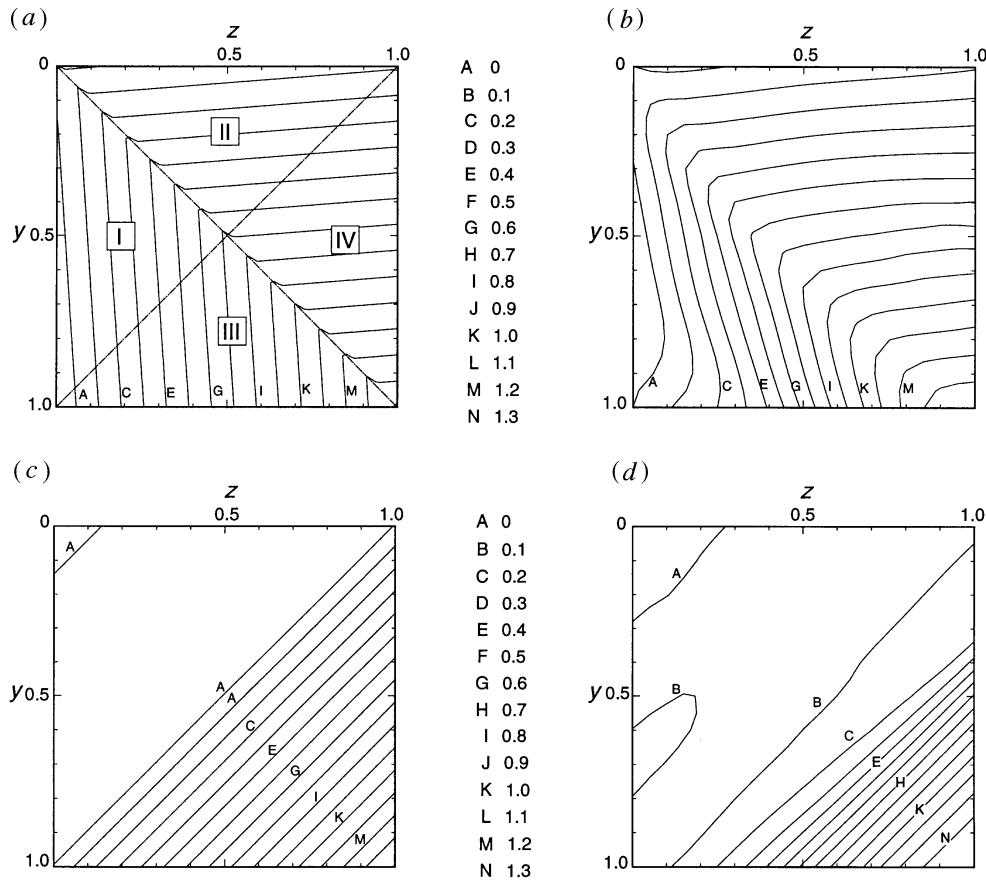


Figure 6. Analytical (a), (c) and finite element (b), (d) velocity distributions u_α , u_β for $\phi = 9.74^\circ$ ($\theta = 45^\circ$).

present detailed comparisons for $\phi = 9.74^\circ$ ($\theta = 45^\circ$) and $\phi = \theta = 70^\circ$ and briefly review the other cases. Because d is arbitrary in the basic solution (3.75) for function $f(\zeta)$, we choose it in each case to minimize the difference in velocity fields between the analytical and numerical solutions, as measured by parameter r_1 .

(i) $\phi = 9.74^\circ$

This orientation (precisely, $b = 4 + 3\sqrt{2}$) was chosen because it gives $\theta = 45^\circ$ in the analytical solution (the limiting case in common between (a) and (b) of figure 4); hence, the corresponding lines of tangential velocity discontinuity lie along the diagonals of the crystal. The velocity fields are expressed in terms of f_0 by substituting (3.75) into (3.28) and (3.29) (or (3.30)), with $c = 0.1464$ from the first equation of (3.76). Upon comparing analytical results with final displacement increments (normalized to velocities) from the finite element calculations, we find (using (4.1)) that $d = -0.0145$ gives a minimum value of $r_1 = 0.01483$. Accordingly, the numerical and analytical results may be judged to be in overall good agreement. Figure 6 displays these results for velocities u_α , u_β as contour lines. (In figure 6a, the computer-plotted, steeply sloping short lines connecting contours on either side of the diagonal from upper left to lower right actually represent finite jumps corresponding to the tangential velocity discontinuity given by the first equation of

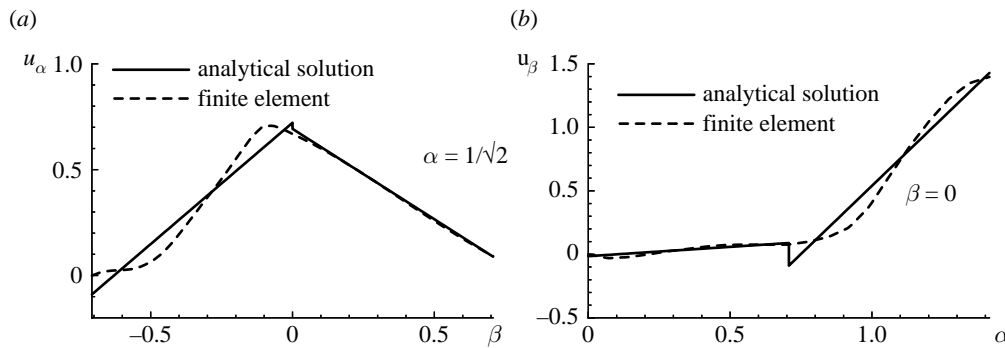


Figure 7. Comparisons along characteristic lines of analytical and finite element results for velocities, $\phi = 9.74^\circ$. (a) u_α along $\alpha = 1/\sqrt{2}$; (b) u_β along $\beta = 0$.

(3.65).) Further comparisons of velocities u_α , u_β along the diagonals $\alpha = 1/\sqrt{2}$ and $\beta = 0$ are shown in figure 7. It is seen from this figure that the velocity discontinuity in u_β across the diagonal $\alpha = 1/\sqrt{2}$ extending from the lower left corner is much the stronger of the two discontinuities (0.1926 versus 0.0290 from (3.65), (3.75) and the values for c and d). Prior to having made any numerical studies, we suggested in Wu & Havner (1995, §6) that the necessary tangential velocity discontinuity would emanate from this corner. The general agreement between solutions, save for the intrinsic absence of velocity discontinuities in the finite element results, is evident from figures 6 and 7.

In figure 8a, the distribution of normalized lattice stress $A = (\sigma_{33} - \sigma_{11})/(\sqrt{6}\tau_0)$, from the finite element solution at the end of the elastoplastic transition, is shown. Because the analytical solution corresponds to a stress point on edge AB of the yield locus (figure 2), the analytical result obviously is $A = 0$. From figure 8a, it is seen that, with the exception of a roughly triangular region encompassing and somewhat larger than region II, the finite element A-values are nearly zero. Thus, the agreement with the analytical solution is quite good outside region II. Within that region, recall from §3b(i) that inequality (3.42) governing $f'(\zeta)$ (from normality constraint (3.37)₁, $f'_i + g'_i \geq -1/\sqrt{2}$) may be set as an equality, thereby making $\gamma'_3 = 0$. (The normality constraint is a strict inequality in the other regions from (3.38)–(3.39), with $\gamma'_3 > 0$.) This is precisely what is done in the basic solution (3.75) and the first equation of (3.76). Consequently, *the basic velocity field permits the stress state in region II to lie within face ABCD of the yield locus* (figure 2), rather than be restricted to edge AB. (Of course, the stress state must lie on AB in the other regions because $\gamma'_3 > 0$.) Thus, although we only have found an analytical solution for the stress state that is uniform, it is conceivable, given the elastoplastic finite element results, that there may be an alternative non-uniform stress state in the rigid-plastic crystal which extends into the interior of yield face ABCD in region II. Moreover, since only the basic solution (3.75) (with the first equation of (3.76)) permits this (for $A \equiv 0$ otherwise), the finite element results appear to reinforce our choice of that solution. The corresponding distribution on the yield face of the finite element stresses is shown in figure 8b.

The finite element results for final lattice-rotation rate ϕ' are shown in figure 8c. This continuous distribution is, of course, not consistent with maintaining lattice integrity in finite regions (i.e. subgrains). Nevertheless, subgrains can be roughly defined, particularly one in region II. The deformed shape of the right-hand crystal

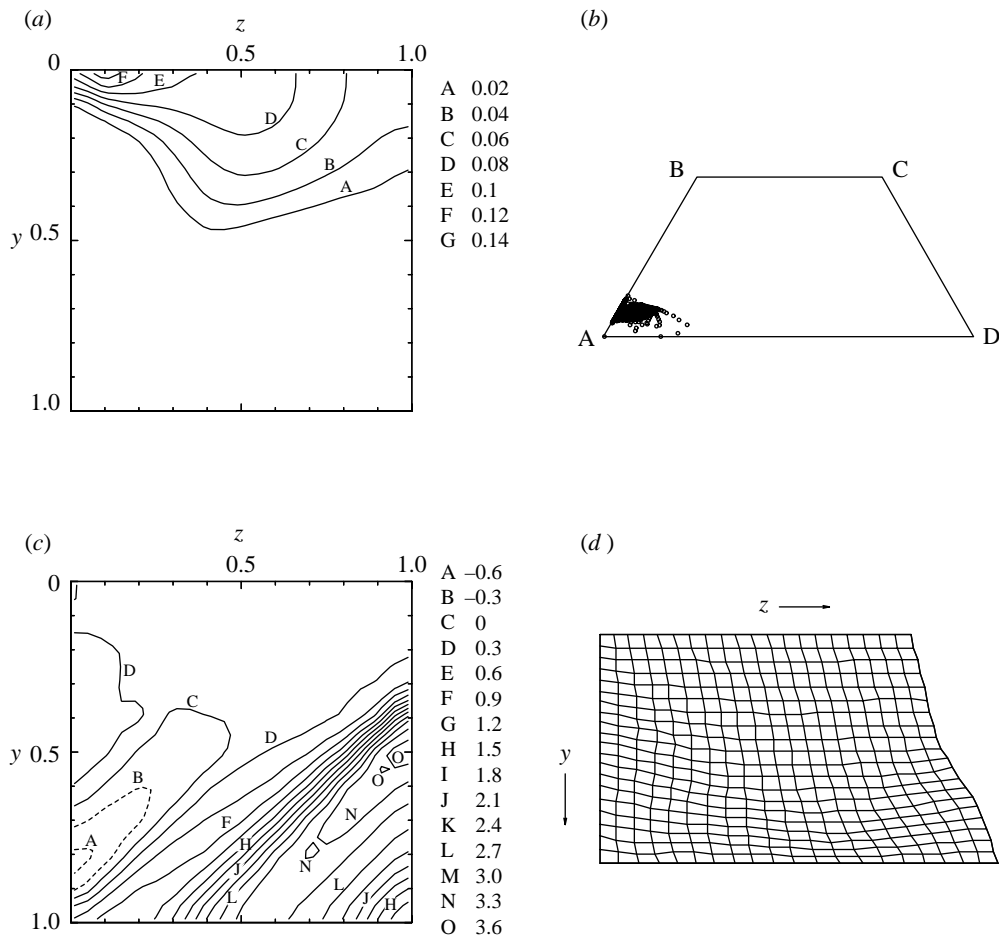


Figure 8. Finite element results for $\phi = 9.74^\circ$. (a) Normalized stress $A = (\sigma_{33} - \sigma_{11}) / (\sqrt{6}\tau_0)$; (b) distribution of stress state on yield locus; (c) lattice-rotation rate ϕ' (radians per unit logarithmic compressive strain ϵ_L); (d) deformed shape (greatly exaggerated) of right-hand crystal.

at the end of the elastoplastic transition is shown (to a greatly exaggerated scale) in figure 8d. The apparent beginning of narrow bands of intense shearing approximately lying along the main diagonals can be seen; and another shear band which intersects the midpoint of the free edge appears to be forming nearly parallel to the lower-left / upper-right diagonal. The former bands are roughly comparable to the analytical tangential velocity discontinuities, but the latter band has no counterpart in the analytical solution.

Figures 9 and 10 show the finite element results for the σ_{xx} , σ_{yy} , σ_{zz} and σ_{yz} distributions at the beginning and end, respectively, of the elastoplastic transition (the dashed lines indicating negative values). The integrated σ_{xx} stresses from figure 10a, compared with $f_0 = 4.42\tau_0$ from (3.14), give $r_2 = 0.9995$ or a yield-point load only 0.05% smaller than the analytical solution (as previously noted). However, the non-uniformity of the distribution has increased during the elastoplastic stage, contrary to our expectations (since our analytical solution gives a uniform state). The σ_{yz} stress (figure 10d) remains quite small (on average only a few percent of σ_{xx} values), but σ_{zz} (figure 10c) increases to values as large as 20% of σ_{xx} . These

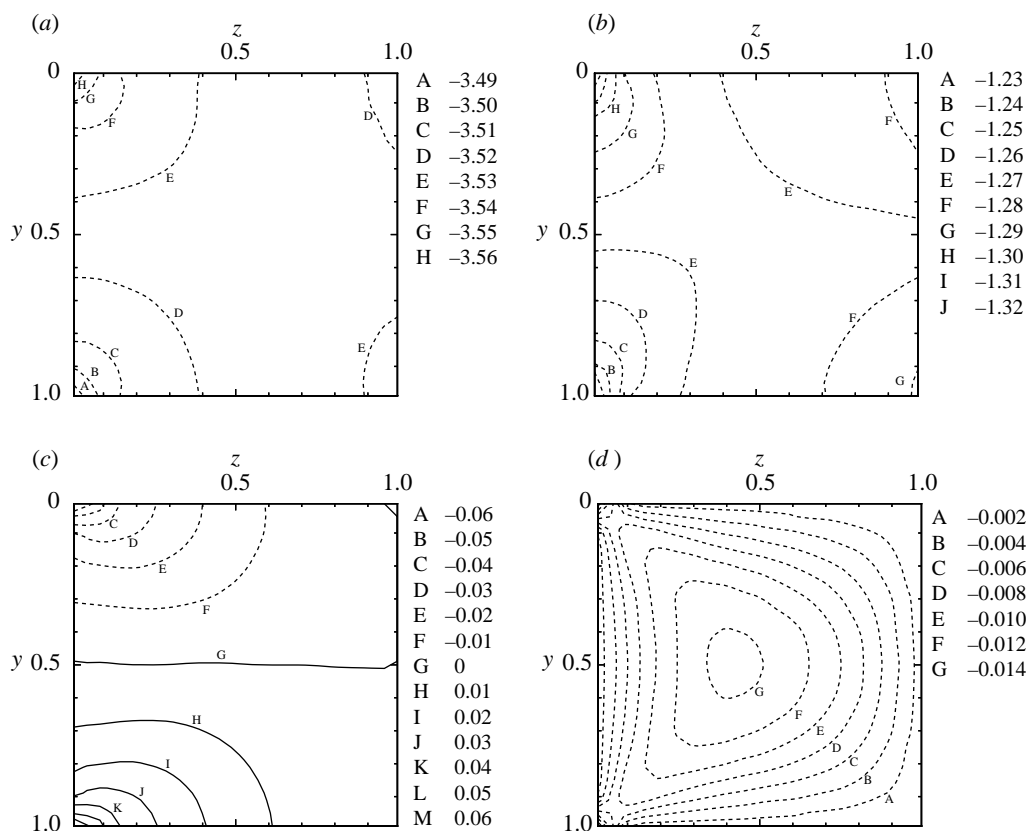


Figure 9. Finite element results for stresses (divided by τ_0) at the beginning of the elastoplastic transition, $\phi = 9.74^\circ$. (a) σ_{xx} , (b) σ_{yy} , (c) σ_{zz} , (d) σ_{yz} .

stresses are, of course, zero in the analytical solution. The final σ_{yy} stress ranges between $-1.85\tau_0$ and $-2.70\tau_0$, while the uniform analytical result is $-2.31\tau_0$, from the second equation of (3.14). The calculated parameter $r_3 = 0.992$, indicating the elastic strain increments are very nearly zero at the end of the finite element calculations. (The calculations actually stopped when the stress state at a material point near the (1, 0) corner of the crystal reached vertex A of the yield locus, where the elastoplastic stiffness matrix is singular.)

(ii) $\phi = 70^\circ$

This range III orientation is near the middle of the subrange (67.5 – 72.07°), in which the crystal separates from the channel wall along $y = 1$ (§ 3d). Moreover, it is within the narrow range (69.79 – 70.40°), for which it is possible to have an analytical solution with no tangential velocity discontinuities (§ 3e and the fourth equation of (3.76)). This is the solution presented and compared with finite element results in Wu (1995, § 5.4, case (4)). It differs relatively little from that of table 2, which solution has only small velocity discontinuities as we shall see. For this latter solution, the corresponding velocity fields are obtained by substituting (3.75) into (3.51), (3.53) and (3.60), with $c = 0.2387$, $m_1 = 2.747$ and $m_2 = 0.3073$, from table 2. (The values from the continuous solution (the fourth equation of (3.76)) and (3.57) are $c = 0.2778$ and $m_2 = 0.2977$, with $m_1 = \tan 70^\circ = 2.747$, as before.) Comparing

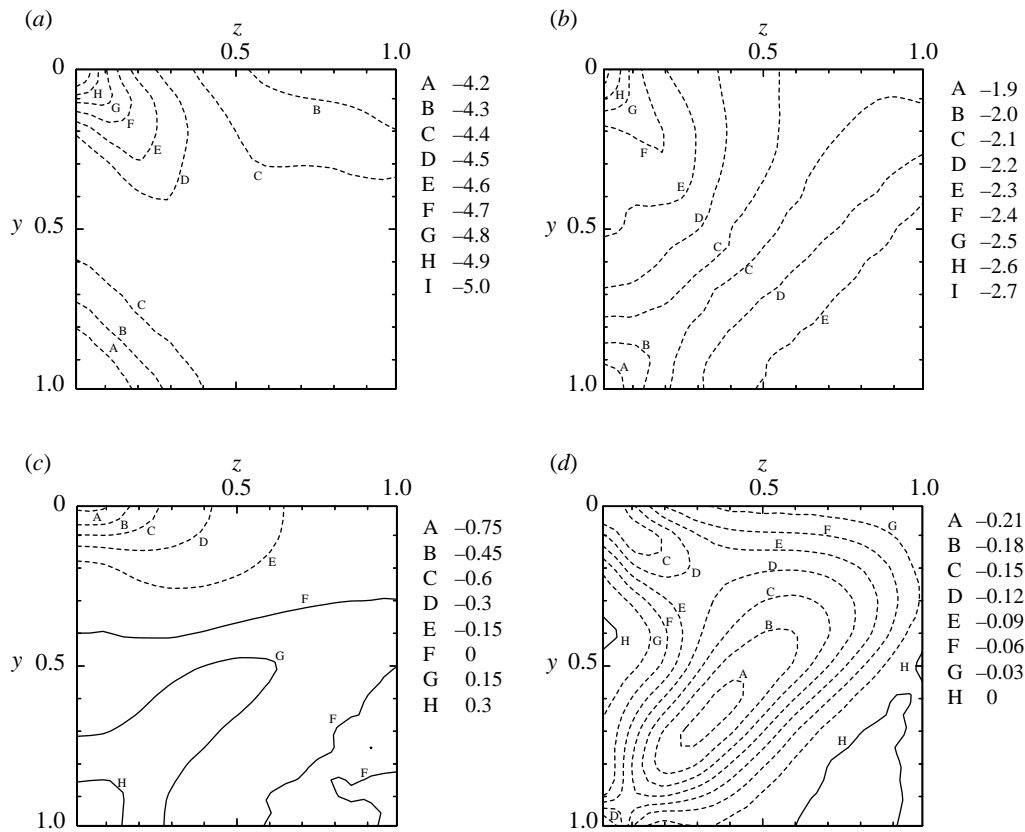


Figure 10. Finite element results for stresses (divided by τ_0) at the end of the elastoplastic transition, $\phi = 9.74^\circ$. (a) σ_{xx} , (b) σ_{yy} , (c) σ_{zz} , (d) σ_{yz} .

analytical results based on table 2 with final values from the finite element method for this orientation, we find that $d = 0.00653$ gives the minimum $r_1 = 0.00815$ (from (4.1)). (In Wu (1995), the continuous solution requires $d = f(0) = 0$ and the comparison with finite element results gives $r_1 = 0.00729$.) Recall that in the previous case, $r_1 = 0.01483$. Thus, the numerical and analytical results for velocity fields (from either solution) are closer overall for $\phi = 70^\circ$ than for $\phi = 9.74^\circ$.

Results for velocities u_α , u_β are shown in figure 11. Analytical results for the continuous velocity field (Wu 1995, figure 31) are distinguishable visually from the present solution (table 2) only by the absence from Wu's figure of the small discontinuity in u_α across the characteristic line ($\beta = 0$) extending from the upper left corner (figure 11a). (The discontinuity is represented by steep, short lines connecting the two sets of contours in the computer-plotted figure.) There also is a tangential velocity discontinuity across the line separating regions IV and V (figure 11a), which is too small to be visible at this scale. The u_α , u_β velocities along characteristics $\alpha = \cos 70^\circ = 0.3420$ and $\beta = 0$ are shown in figure 12 for all three solutions. It is seen that for the present analytical solution, labelled A in the figure, the discontinuity in u_β across the characteristic line ($\alpha = 0.3420$) extending from the lower left corner is much smaller than that in u_α across the line $\beta = 0$ from the upper left corner (0.00129 versus 0.0203 from (3.67), (3.75) and the c , d and m_2 values). This is in contrast to the range I case, $\phi = 9.74^\circ$, where also the maximum discontinuity

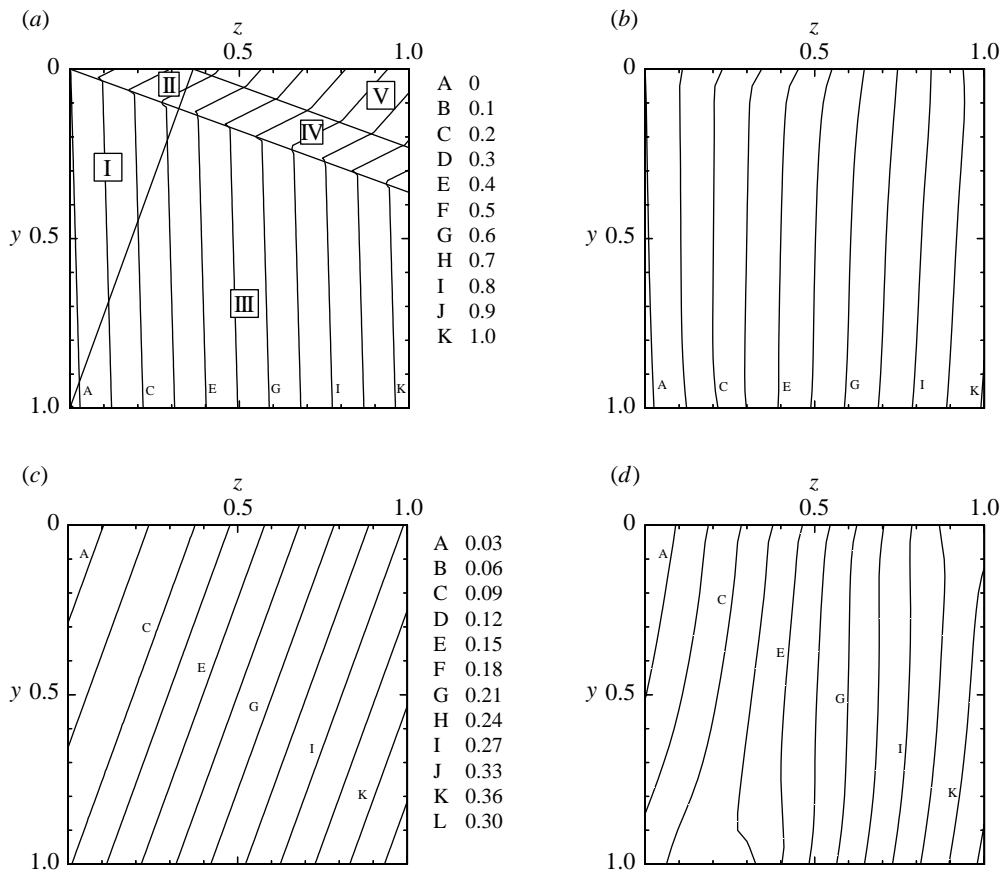


Figure 11. Analytical (a), (c) and finite element (b), (d) velocity distributions u_α , u_β for $\phi = \theta = 70^\circ$.

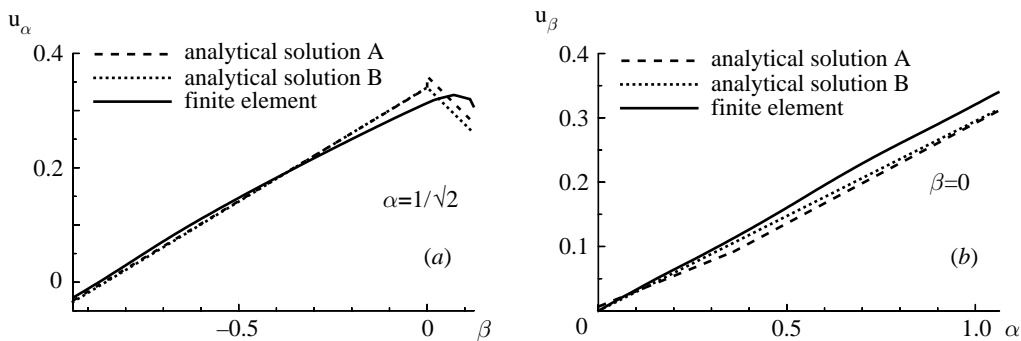


Figure 12. Comparisons along characteristic lines of two analytical solutions with finite element results for velocities, $\phi = 70^\circ$. (a) u_α along $\alpha = \cos 70^\circ$, (b) u_β along $\beta = 0$. ('A' corresponds to the present solution, table 2. 'B' corresponds to that of Wu (1995), represented by equations (3.76).)

is an order-of-magnitude larger. The tangential velocity discontinuity in u_α across the line between regions IV and V is a decrease of 0.00354.

The distribution of normalized stress $B = \sigma_{13}/(\sqrt{6}\tau_0)$ at the end of the finite element calculations is shown in figure 13*a*. Although at first glance these results may not appear close to the analytical solution $B = 0$ (edge AD of the yield locus, figure 2), nevertheless they are. The largest value is only slightly above the 0.055 contour line, whereas the intensity of the normalized load $f_0/(\sqrt{6}\tau_0)$ is 1.0 from the first equation of (3.16). This closeness of numerical and analytical results is much more apparent in figure 13*b*, where the distribution on the yield face ABCD of the finite element stress state is shown. (The analytical solution corresponds to the midpoint of edge AD.) It may be recalled from §3*d*, figure 5 and (3.58), that the analytical solution with tangential velocity discontinuities presented here (but not the continuous solution) satisfies the upper bound normality constraint $f'_i + g'_i = 1/\sqrt{2}$ in region III, whence γ'_9, γ'_{10} are zero in this large portion (65.7%) of the crystal. Therefore, it again is conceivable that a non-uniform stress state may exist in the rigid-plastic crystal which extends into the interior of face ABCD, in this case within region III. (The upper-bound constraints are strict inequalities in the other regions, giving $\gamma'_9 > 0$ and so requiring those stress states to lie on edge AD.) Of course, that stress state would have to satisfy $\sigma_{yy} = 0$ along $y = 1$ because of the separation from the channel wall. It is worth noting from figure 13*a* that the larger values of B (0.03 and above) are encompassed within an area approximated by region III.

In figure 13*c* are shown the results for lattice-rotation rate ϕ' at the end of the finite element calculations. This distribution roughly approximates the analytical solution $\phi' = -0.3956$ in regions I and II (from (3.77)). However, it has only a very small region of positive ϕ' , whereas the analytical solution gives a positive rate throughout the other three regions. The deformed shape from the finite element results (as before, to a greatly exaggerated scale) is shown in figure 13*d*. The numerical solution also gives a displacement of the crystal face away from the wall (as is clearly evident if a straight edge is placed along the lower edge of the figure), but only over approximately 25% of the length. (The analytical solution, in contrast, predicts separation up to corner (1, 1) from (3.64)₁). Only a very vivid imagination might suggest the beginning of a shearing band along the characteristic direction $\beta = 0$.

Finite element results for stresses $\sigma_{xx}, \sigma_{yy}, \sigma_{zz}$ and σ_{yz} at both the beginning and end of the elastoplastic transition are shown in figures 14–15. The resultant of the σ_{xx} distribution compared with $f_0 = \sqrt{6}\tau_0$ (from (3.16)) gives $r_2 = 0.9785$, whence the final load is 2.15% smaller than the analytical value. As in the previous case ($\phi = 9.74^\circ$), the numerical stress state has become more non-uniform during this stage and the final σ_{yy}, σ_{zz} and σ_{yz} stresses are not very close to their analytical values, which are zero. However, one may note that the final magnitudes of σ_{yy} are reduced significantly toward zero from their purely elastic values. No stress point reached a singularity, as evident from figure 13*b*, and the convergence criterion in the computer code ended the calculations at $r_3 = 1.008$ (from (4.3)). Thus, most of the final elastic strain increments had opposite signs from the very much larger plastic strain increments.

As mentioned at the beginning of §4*b*, numerical results for $\phi = 45^\circ, 60^\circ$ and 80° are also given in Wu (1995, §5.4). For $\phi = 80^\circ$, there is no separation from channel walls (§3*c*) and the good agreement between analytical and finite element solutions is comparable to that for $\phi = 70^\circ$. The r -values are: $r_1 = 0.01081$, $r_2 = 0.9953$ (a maximum load only 0.47% less than the analytical result) and $r_3 = 1.005$. For $\phi = 60^\circ$, the crystal separates from both channel walls in the analytical solution (§3*d*), but only along $y = 1$ in the finite element results. There are much greater

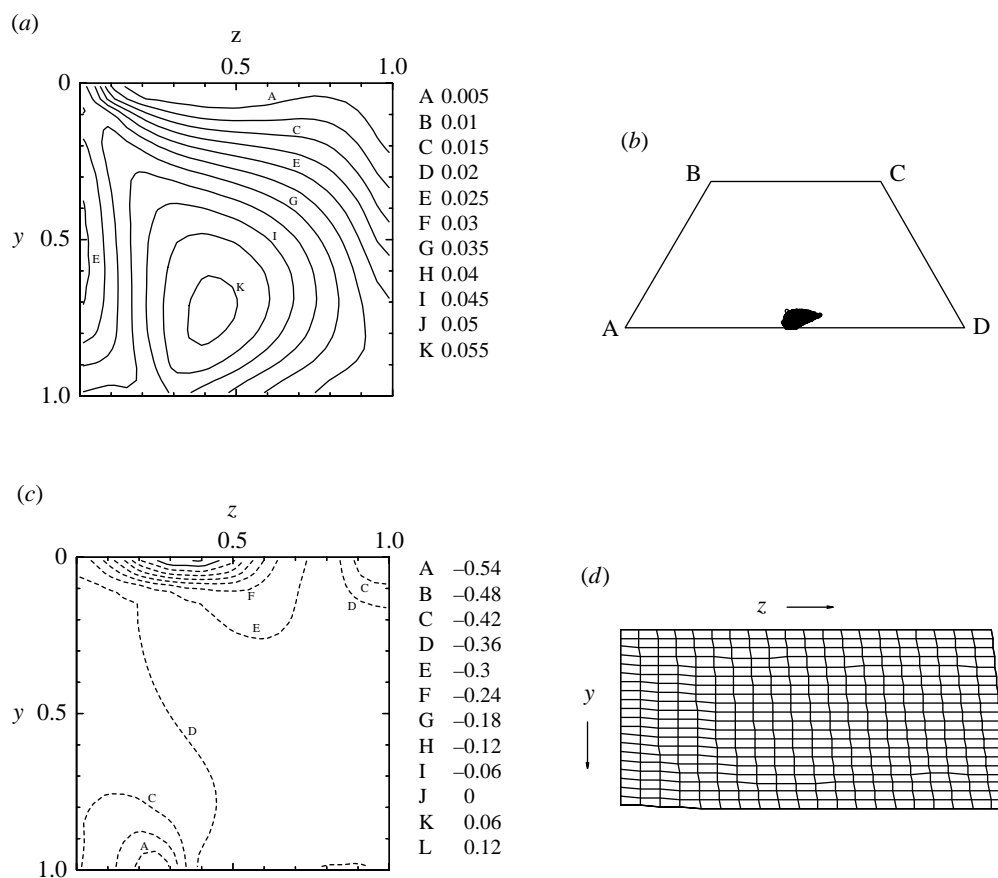


Figure 13. Finite element results for $\phi = 70^\circ$. (a) Normalized stress $B = \sigma_{13}/(\sqrt{6}\tau_0)$; (b) distribution of stress state on yield locus; (c) lattice-rotation rate ϕ' (radians per unit logarithmic compressive strain ϵ_L); (d) deformed shape (greatly exaggerated) of right-hand crystal.

differences between solutions than for the preceding cases, with $r_1 = 0.273$, $r_2 = 1.0161$ and $r_3 = 1.023$. For $\phi = 45^\circ$, the basic analytical solution (3.75)–(3.76) has relatively large tangential velocity discontinuities along the crystal diagonals, but no separation from channel walls in range II (§3*b*). In contrast, the finite element results require separation along 15% of the length from the lower left corner. Consequently, the differences in velocity fields and stress distributions are large for $\phi = 45^\circ$, with $r_1 = 0.381$ (!), $r_2 = 0.9909$ and $r_3 = 1.022$. Thus, for these last two cases, only the analytical and numerical yield-point loads are close (differing by 1.61 and 0.91%, respectively, for $\phi = 60^\circ$ and 45°).

5. Summary and discussion

We have obtained analytical solutions for both non-uniform velocity fields and stress states for all lattice orientations of symmetric, rigid-plastic FCC bicrystals in (110) channel die compression, extending and generalizing results in Wu & Havner (1995) for the range $0 < \phi < 35.26^\circ$ (range I). Although the velocity field is not uniquely determined, *every possible solution requires that there be tangential velocity discontinuities along characteristic directions extending from the interface corners,*

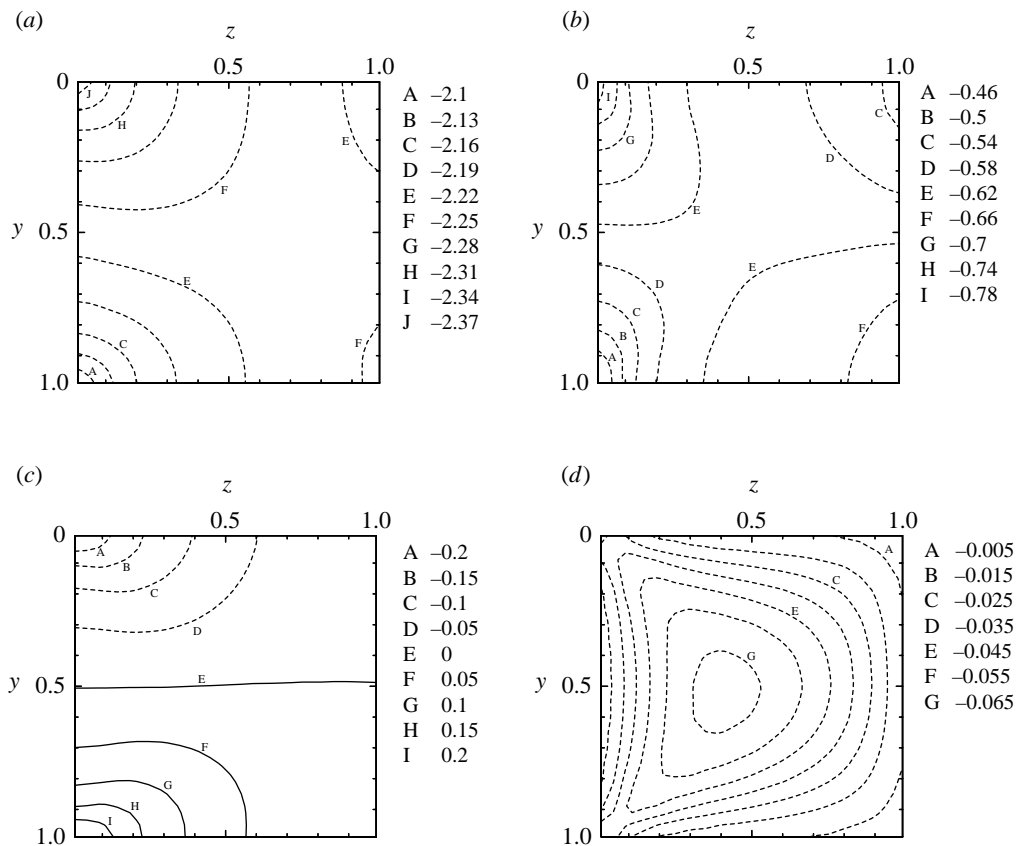


Figure 14. Finite element results for stresses (divided by τ_0) at the beginning of the elastoplastic transition, $\phi = 70^\circ$. (a) σ_{xx} , (b) σ_{yy} , (c) σ_{zz} , (d) σ_{yz} .

with the exception of a very narrow range (less than one degree) of orientations around $\phi = 70^\circ$. The simplest possible solution (consisting of linear velocity fields), which we have called the 'basic solution', maintains the integrity of lattice structure and predicts the initiation of subgrains (i.e. regions of finitely differing lattice-rotation rates). An analytical result which we did not anticipate, and which awaits experimental confirmation (or refutation) from tests on bicrystals in (110) loading, is the requirement that *all bicrystals in the orientation range between 54.74° and 72.07° begin to separate from one or both channel walls.*

The analytical solution for stress, based upon the assumption that the stress state for a given orientation lies along an edge of yield-locus face ABCD in lattice stress space (figure 2), is uniform in every range. However, as we have shown, it may be possible that the basic solution for velocity fields permits a non-uniform stress state lying partly in the yield face and partly on an edge.

We also have compared in detail the analytical solutions with finite element calculations of elastoplastic aluminium bicrystals in two different orientations, $\phi = 9.74^\circ$ (range I) and $\phi = 70^\circ$ (range III), and briefly reviewed comparisons of other orientations in Wu (1995). It was our thought in undertaking numerical studies that the incremental response at the end of the elastoplastic transition could provide insight into the choice of analytical solution (since non-unique) for the rigid-plastic crystal. (Of course, there is an inherent difference because the finite element results

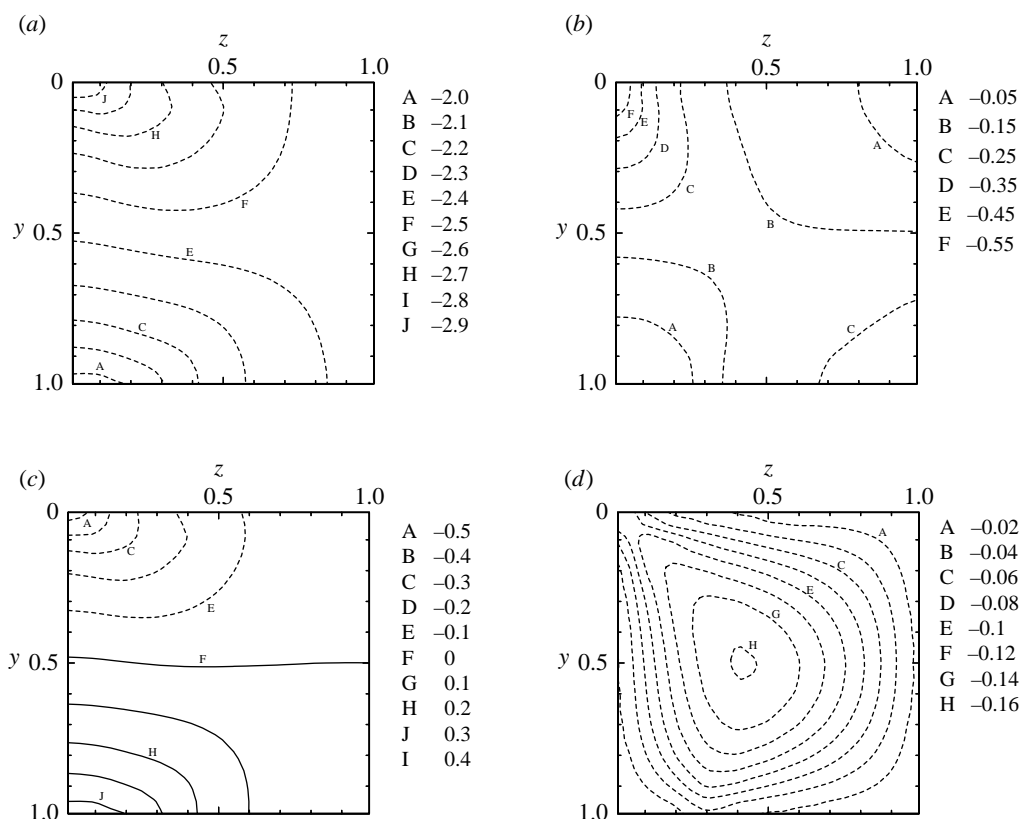


Figure 15. Finite element results for stresses (divided by τ_0) at the end of the elastoplastic transition, $\phi = 70^\circ$. (a) σ_{xx} , (b) σ_{yy} , (c) σ_{zz} , (d) σ_{yz} .

depend upon continuous displacement fields.) For the two cases presented, the numerical results reinforce the basic solution, as they also do in other orientations. However, there are marked differences between the finite element results reported in Wu (1995) and the basic solution for $\phi = 45^\circ$ (the only orientation investigated in range II, $35.26^\circ < \phi < 54.74^\circ$), corresponding to edge BC of the yield locus.

In regard to stresses, the finite element results suggest that, for a given orientation, there may be a non-uniform stress state in the rigid-plastic crystal that gives the same yield-point load (of course) but that lies partly within the yield locus face (as noted above). Moreover, finite element results for $\phi = 45^\circ$ shown in Wu (1995, figure 19), strongly suggest that in range II a more realistic non-uniform stress state may lie on *three* edges of yield-locus face ABCD (contrary to our assumption of edge BC only), as well as within the face. This would mean that the associated velocity field would subdivide the crystal into regions having different characteristic directions (from (3.8)–(3.9)) and different combinations of slip systems (i.e. a_1 , b_2 and c_1 , c_2 for stresses on edge AB, a_1 , b_2 and a_3 , b_3 for edge BC, a_1 , b_2 and a_2 , b_1 for edge AD and a_1 , b_2 only for stresses within face ABCD).

The analytical prediction herein of tangential velocity discontinuities and the initiation of subgrains in a rigid-plastic crystalline slip model at the yield point, based upon Schmid's law (of critical resolved shear stress) and standard FCC crystallographic slip systems, seems to indicate that grain boundaries play a role in subgrain and shearband formation in polycrystalline metals. In the present bicrystal model,

which obviously does not consider metallurgical factors below the level of continuum slip, the interface constraint creates tangential velocity discontinuities as geometrically necessary interior boundaries separating regions of differing strain-rates and lattice-rotation rates. These are all strict consequences of satisfying the kinematic boundary conditions of the rigid channel die and the polyhedral yield-locus normality constraints corresponding to FCC slip-system geometry (which constraints represent neither more nor less than the classical perspective that a slip system can be active only if its critical shear strength is attained by the local stress state). In general, four slip systems are active in each region. This number appears to be consistent with the experimental finding for cell-forming metals quoted (from Bay *et al.* 1992) in the Introduction, which also applies to non-cell forming metals (Hughes 1993). That is, fewer slip systems are active in individual (subgrain) regions than the Taylor criterion specifies (which number of course is five). A notable difference with the cited polycrystalline experimental behaviour, however, is that the observed cell-block walls (Bay *et al.* 1992) and domain boundaries (Hughes 1993) intersect at approximately 60° angles, whereas in the theoretical predictions for the bicrystal model (for any orientation range) all interior boundaries are orthogonal from the general relations (3.25).

Because of the finitely differing lattice-rotation rates across various interior lines (i.e. ab, oc and bd or cd, figure 4) at the yield point, boundary conditions for all regions will have changed slightly after a very small strain increment. Consequently, we anticipate that solution (3.26) for u_α and u_β (which always holds locally for the bicrystal model) will further subdivide the regions due to the incrementally different θ 's, thereby initiating the formation of additional (and smaller) subgrains, and that this process will continue. To speculate further, however, is inappropriate since prediction of the evolution of subgrains and shear bands (from tangential velocity discontinuities) requires a difficult mathematical analysis beyond the scope of the present paper. One of us (K.S.H.) intends to undertake an analysis (with appropriate crystal hardening rules) of the early stages of that evolution, perhaps guided by the second-order investigation of single crystal deformation in Havner (1984) and Havner & Sue (1985).

We thank the National Science Foundation, Mechanics and Materials Program, for support of this work through Grant CMS-9414376. Cray Y-MP time was provided by the North Carolina Supercomputing Center.

References

- Bay, B., Hansen, N., Hughes, D. A. & Kuhlmann-Wilsdorf, D. 1992 Evolution of f.c.c. deformation structures in polyslip. *Acta Metall. Mater.* **40**, 205–219.
- Bay, B., Hansen, N. & Kuhlmann-Wilsdorf, D. 1989 Deformation structures in lightly rolled pure aluminium. *Mater. Sci. Engng A* **113**, 385–397.
- Chester, C. R. 1972 *Techniques in partial differential equations*. New York: McGraw-Hill.
- Chidambarrao, D. & Havner, K. S. 1988a Finite deformation analysis of f.c.c. crystals in $(110)(\bar{1}\bar{1}\bar{2})(\bar{1}\bar{1}\bar{1})$ channel die compression. *Int. J. Plasticity* **4**, 1–27.
- Chidambarrao, D. & Havner, K. S. 1988b On finite deformation of f.c.c. crystals in (110) channel die compression. *J. Mech. Phys. Solids* **36**, 285–315.
- Chin, G. Y., Nesbitt, E. A. & Williams, A. J. 1966 Anisotropy of strength in single crystals under plane strain compression. *Acta Metall.* **14**, 467–476.
- Driver, J. H. & Skalli, A. 1982 L'essai de compression plane de monocristaux encastres: methode d'étude du comportement d'un cristal soumis à une deformation plastique imposée. *Rev. Phys. Appl.* **17**, 447–451.

Non-uniform straining and subgrain initiation in bicrystals 1943

- Fuh, S. 1989 Applications of a postulate of minimum plastic spin in crystal mechanics. Ph.D. thesis, North Carolina State University.
- Fuh, S. & Havner, K. S. 1986 On uniqueness of multiple-slip solutions in constrained and unconstrained f.c.c. crystal deformation problems. *Int. J. Plasticity* **2**, 329–345.
- Fuh, S. & Havner, K. S. 1989 A theory of minimum plastic spin in crystal mechanics. *Proc. R. Soc. Lond. A* **422**, 193–239.
- Havner, K. S. 1971 A discrete model for the prediction of subsequent yield surfaces in polycrystalline plasticity. *Int. J. Solids Struct.* **7**, 719–730.
- Havner, K. S. 1984 First- and second-order analysis of axially loaded crystals in n -fold symmetry. *Phil. Trans. R. Soc. Lond. A* **311**, 469–493.
- Havner, K. S. 1992 *Finite plastic deformation of crystalline solids*. Cambridge University Press.
- Havner, K. S. & Chidambarrao, D. 1987 Analysis of a family of unstable lattice orientations in (110) channel die compression. *Acta Mech.* **69**, 243–269.
- Havner, K. S. & Sue, P. L. 1985 Theoretical analysis of the channel die compression test. II. First- and second-order analysis of orientation $[110][00\bar{1}][\bar{1}10]$ in f.c.c. crystals. *J. Mech. Phys. Solids* **33**, 285–313.
- Havner, K. S. & Wu, S.-C. 1995 An analytical investigation of inhomogeneous straining, subgrain formation, and the initiation of microshear bands in bicrystals. In *Proc. IUTAM Symp. on Anisotropy, Inhomogeneity and Nonlinearity in Solid Mechanics* (ed. D. F. Parker & A. H. England), pp. 211–216. Dordrecht: Kluwer.
- Havner, K. S., Wu, S.-C. & Fuh, S. 1994 On symmetric bicrystals at the yield point in (110) channel die compression. *J. Mech. Phys. Solids* **42**, 361–379.
- Hu, X., Wei, C., Margolin, H. & Nourbakhsh, S. 1993 The stresses in a face-centered cubic single crystal under uniaxial tension. *Metall. Trans. A* **24**, 875–881.
- Hughes, D. A. 1993 Microstructural evolution in a non-cell forming metal: Al-Mg. *Acta Metall. Mater.* **41**, 1421–1430.
- Hughes, D. A. & Nix, W. D. 1989 Strain hardening and substructural evolution in Ni-Co solid solutions at large strains. *Mater. Sci. Engng A* **122**, 153–172.
- Kocks, U. F. & Chandra, H. 1982 Slip geometry in partially constrained deformation. *Acta Metall.* **30**, 695–709.
- Nye, J. F. 1957 *Physical properties of crystals*. Oxford University Press.
- Skalli, A. 1984 Etude théorique et expérimentale de la déformation plastique en compression plane de cristaux d'aluminium. Thèse d'Etat, Ecoles des Mines de St. Etienne.
- Skalli, A., Driver, J. H. & Wintenberger, M. 1983 Etude théorique et expérimentale de la déformation plastique de monocristaux d'aluminium. Deuxième partie: compression plane partiellement imposée. *Mem. Et. Sci. Revue Metall.* **80**, 293–302.
- Sue, P. L. & Havner, K. S. 1984 Theoretical analysis of the channel die compression test. I. General considerations and finite deformation of f.c.c. crystals in stable lattice orientations. *J. Mech. Phys. Solids* **32**, 417–442.
- Wonsiewicz, B. C. & Chin, G. Y. 1970 Plane strain compression of copper, Cu 6Wt Pct Al, and Ag 4Wt Pct Sn crystals. *Metal. Trans.* **1**, 2715–2722.
- Wonsiewicz, B. C., Chin, G. Y. & Hart, R. R. 1971 Lateral constraints in plane strain compression of single crystals. *Metall. Trans.* **2**, 2093–2096.
- Wu, S. C. 1995 Analysis of symmetric bicrystals in (110) channel die compression. Ph.D. thesis, North Carolina State University.
- Wu, S. C. & Havner, K. S. 1995 Exact stress states and velocity fields in bicrystals at the yield point in channel die compression. *Z. Angew. Math. Phys.* **46**, S446–S465.

Received 13 October 1995; revised 7 June 1996; accepted 17 July 1996

MATHEMATICAL,
PHYSICAL
& ENGINEERING
SCIENCES

THE ROYAL
SOCIETY

PHILOSOPHICAL
TRANSACTIONS
OF

MATHEMATICAL,
PHYSICAL
& ENGINEERING
SCIENCES

THE ROYAL
SOCIETY

PHILOSOPHICAL
TRANSACTIONS
OF